

Faster Convergence in Deep-Predictive-Coding Networks to Learn Deeper Representations

Isaac J. Sledge, *Member, IEEE*, and José C. Príncipe, *Life Fellow, IEEE*

Abstract—Deep-predictive-coding networks (DPCNs) are hierarchical, generative models that rely on feed-forward and feed-back connections to modulate latent feature representations of stimuli in a dynamic and context-sensitive manner. A crucial element of DPCNs is a forward-backward inference procedure to uncover sparse states of a dynamic model, which are used for invariant feature extraction. However, this inference and the corresponding backwards network parameter updating are major computational bottlenecks. They severely limit the network depths that can be reasonably implemented and easily trained. We therefore propose a optimization strategy, with better empirical and theoretical convergence, based on accelerated proximal gradients.

We demonstrate that the ability to construct deeper DPCNs leads to receptive fields that capture well the entire notions of objects on which the networks are trained. This improves the feature representations. It yields completely unsupervised classifiers that surpass convolutional and convolutional-recurrent autoencoders and are on par with convolutional networks trained in a supervised manner. This is despite the DPCNs having orders of magnitude fewer parameters.

Index Terms—Bio-inspired vision, predictive coding, unsupervised learning

1. Introduction

Predictive coding is a promising theory for sensory information processing. Under this theory, a dynamics-based hierarchical, generative model [1, 2] of the world is formed and consistently updated to infer the possible physical causes of given stimuli while suppressing prediction errors at all levels [3]. Top-down connections carry predictions about activity, in the form of the causes, to the lower model levels. The propagated causes reflect past experience [4] and act as priors to disambiguate the incoming sensory inputs. Bottom-up connections relay prediction errors to higher levels to update the causes. The interaction of the feed-forward and feed-back connections [5] on the causes enables robust object analysis [6] from the observed stimuli.

Several predictive coding schemes have been created and their biological plausibility investigated [1, 4, 7, 8]. None of the early contributions, however, have been known to extract highly discriminative details, like sparse, invariant feature representations, that are helpful for high-level object analysis tasks. Our lab thus developed multi-layer, deep-predictive-coding networks (DPCNs) [9–11]; alternate networks later followed [12, 13].

DPCNs can be thought of as parameter-light, non-traditional autoencoders with feed-forward and recurrent feed-back connections. They do not have a corresponding decoder, though, so they require a self-organizing principle to be effective.

During training, DPCNs learn, according to a free-energy principle [14], to build spatio-temporal, transformation-invariant representations of dynamic input stimuli [15]. This yields an approximate identity mapping that preserves perceptual difference. The underlying feature representations are composed of hidden states and causes. Hidden states describe conditional dependencies over time in the stimuli. Hidden causes are transform-invariant versions of the states that mediate conditional state dependencies. For static input stimuli, DPCNs behave similarly to sparse-coding models [16].

DPCNs have exhibited promise for implementing unsupervised object recognition in images and video, especially when the objects are well localized throughout space and time. It has been demonstrated that DPCNs learn sparse features that are better for classification than those from alternate convolutional and deconvolutional autoencoders on many benchmark datasets. Such behavior stemmed from the interaction of feed-forward and feed-back connections in the networks. It also arose due to the implicit supervision imposed from leveraging temporal information [17]. Moreover, multiple presentations of the stimuli facilitated the extraction of spatial and temporal regularities [18, 19], which we hypothesize permitted high-level object analysis [20], like class recognition.

Isaac J. Sledge is the Senior Machine Learning Scientist with the Advanced Signal Processing and Automated Target Recognition Branch, Naval Surface Warfare Center, Panama City, FL, USA (email: isaac.j.sledge@navy.mil). He is the director of the Machine Intelligence Defense (MIND) lab at the US Naval Sea Systems Command.

José C. Príncipe is the Don D. and Ruth S. Eckis Chair and the Distinguished Professor with both the Department of Electrical and Computer Engineering and the Department of Biomedical Engineering, University of Florida, Gainesville, FL, USA (email: principe@ufl.edu). He is the director of the Computational NeuroEngineering Laboratory (CNEL) at the University of Florida.

The work of the authors was funded by grants N00014-14-1-0542 (Marc Steinberg, ONR35), N00014-19-WX-00636 (Marc Steinberg, ONR35), and N00014-21-WX-00476 (J. Tory Cobb, ONR32) from the US Office of Naval Research. The first author was also supported by in-house laboratory independent research (ILIR) grant N00014-19-WX-00687 (Frank Crosby) from the US Office of Naval Research and a Naval Innovation in Science and Engineering (NISE) grant from NAVSEA.

Learning sufficiently robust features in a DPCN has been shown to be quite computationally intensive, though. A multi-stage optimization strategy, based on proximal gradients [21, 22], was used in [9–11] to conduct feed-forward and feed-back inference. Sub-quadratic function-value convergence rates were theoretically guaranteed for this strategy [23, 24], but only sub-linear rates were ever obtained due to severe oscillations; that is, the search was not a descent strategy and could lead to localized increases in the cost function across iterations. The DPCNs were thus practically limited to two layers, which, while sufficient for characterizing certain stimuli, may not yield representations that handle objects in complex environments. The networks exhibited poor empirical performance when extended beyond two layers due to being stymied by the lack of a reasonable convergence rate [25]. That is, the deeper layers did not reach a stable feature representation, which impacted the representations in preceding layers.

Here, we propose an alternate optimization approach for DPCNs to go beyond the two-layer network limitation. We replace the proximal gradient search with an accelerated version (see section 2). This approach possesses a sub-polynomial rate of function-value convergence and largely avoids cost rippling, thereby greatly improving the empirical convergence rate (see section 2). We are thus able to efficiently train both deeper and wider networks that stabilize well. The resulting deeper feature representations are far more robust than those previously obtained for DPCNs. In particular, the later-layer causes have receptive fields that embody the entirety of the objects being presented, despite the lack of training labels, on a variety of benchmark datasets. This yields unsupervised classifiers that are on par with supervised-trained convolutional and convolutional-recurrent deep networks (see section 3). The DPCNs have orders of magnitude fewer parameters, though, than these other deep networks.

2. Deep Predictive Coding

The objective of predictive coding is to approximate external sensory stimuli using generative, latent-variable models. Such models hierarchically encode only the residual prediction errors so that the internal representations are modified only for unexpected changes in the stimuli. The prediction errors are the differences between either the actual stimuli or a transformed version of it and the predicted stimuli produced from the underlying latent variables; we refer to these latent variables as causes.

Definition 1. Let $y_t \in \mathbb{R}^p$ represent a time-varying sensory stimulus at time t . The stimuli can be described by an underlying cause, $\kappa_{1,t} \in \mathbb{R}^{d_1}$, and a time-varying intermediate state, $\gamma_{1,t} \in \mathbb{R}_+^{k_1}$, through a pair of θ -parameterized mapping functions, $f_1 : \mathbb{R}_+^{k_1} \rightarrow \mathbb{R}^p$, the cause-update function, and $g_1 : \mathbb{R}_+^{k_1} \times \mathbb{R}^{d_1} \rightarrow \mathbb{R}_+^{k_1}$, the state-transition function. These functions define a latent-variable model,

$$y_t = f_1(\gamma_{1,t}; \theta) + \epsilon_{1,t}, \quad \gamma_{1,t} = g_1(\gamma_{1,t-1}, \kappa_{1,t}; \theta) + \epsilon'_{0,t}.$$

Here, $\epsilon_{1,t} \in \mathbb{R}^p$ and $\epsilon'_{1,t} \in \mathbb{R}^{k_1}$ are noise terms that represent the stochastic and model uncertainty, respectively, in the predictions. This model can be extended to a multi-layer hierarchy by cascading additional θ -parameterized mapping functions, $f_i : \mathbb{R}_+^{k_i} \rightarrow \mathbb{R}^{d_{i-1}}$ and $g_i : \mathbb{R}_+^{k_i} \times \mathbb{R}^{d_i} \rightarrow \mathbb{R}_+^{k_i}$, at each layer i beyond the first,

$$\kappa_{i-1,t} = f_i(\gamma_{i,t}; \theta) + \epsilon_{i,t}, \quad \gamma_{i,t} = g_i(\gamma_{i,t-1}, \kappa_{i,t}; \theta) + \epsilon'_{i,t}.$$

Here, $\kappa_{i,t} \in \mathbb{R}^{d_i}$, $\gamma_{i,t} \in \mathbb{R}_+^{k_i}$, $\epsilon_{i,t} \in \mathbb{R}^{d_{i-1}}$ and $\epsilon'_{i,t} \in \mathbb{R}^{k_i}$.

For a hierarchical, predictive-coding model, both feed-forward, bottom-up and feed-back, top-down processes are used to characterize observed stimuli. In the former case, the observed stimuli are propagated, in a feed-forward fashion through the model, to extract progressively abstract details. The stimuli are first converted to a series of states that encode spatio-temporal relationships. These states are then made invariant to various transformations, thereby forming the hidden causes. The causes at lower layers of the model form the observations to the layers above. Hidden causes therefore provide a link between the layers. The states, in contrast, both connect the dynamics over time, to ignore temporal discontinuities [26], and mediate the effects of the causes on the stimuli [4]. In the latter case, the model generates top-down predictions such that the neural activity at one layer predicts the activity at a lower layer. The predictions from a higher level are sent through feed-back connections to be compared to the actual activity. This yields a model uncertainty error that is forwarded to subsequent layers to update the population activity and improve prediction. Such a top-down process repeats until the bottom-up stimuli transformation process no longer imparts any new information. That is, there are no unexpected changes in the stimuli that the model cannot predict. Once this occurs, if the model is able to synthesize the input stimuli accurately using the uncovered features, then it means that it has previously seen a similar observation [27].

In the remainder of this section, we propose an efficient architecture for this hierarchical, latent-variable model that is suitable for uncovering discriminative details from the stimuli. We consider a convolutional, accelerated DPCN (ADPCN) that can extract highly sparse, invariant features for either dynamic or static stimuli (see section 2.1). We then show how to effectively infer the ADPCN's latent variables using a fast proximal gradient scheme (see section 2.2). This optimization process permits effectively forming deep hierarchies. Theoretical convergence properties are presented in the online appendix (see appendix A).

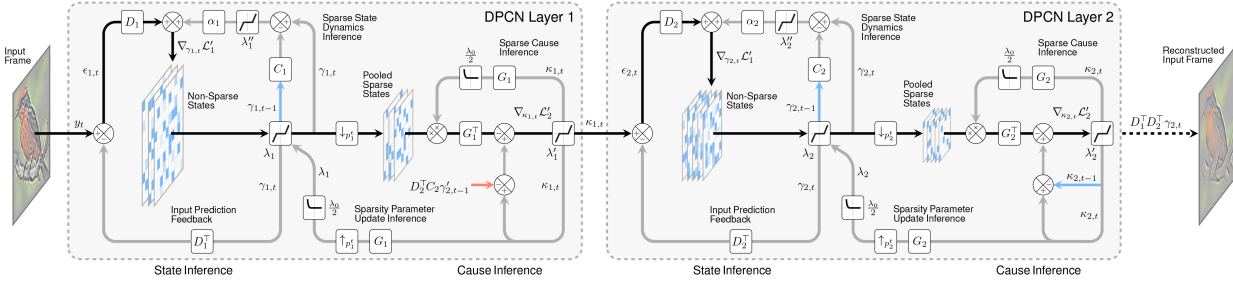


Figure 1: An overview of the DPCN architecture, which, for simplicity, is presented for only two layers. Note that the final layer of the DPCN has no output, unlike in a standard autoencoder network. The goal of the DPCN is to learn a series of causes that explain the input stimuli, in this case, frames from a video of a bird, and hence recreate them. Each layer can be roughly decomposed into two inference blocks, one for updating the states and the other for updating the causes. State and causal inference relies on intra-layer feed-forward (black lines) and feed-back processes (gray lines), along with intra-layer recurrent feed-back (blue lines). Much of the network is devoted to feed-back processes to provide self supervision. Inter-layer feed-back (red line) is used to update the sparsity parameter for the states. For the inference process, we denote multiplication of a quantity on a given path with a rounded square. Addition, subtraction, and multiplication of quantities along multiple paths are denoted using circular gated symbols. Pooling and un-pooling are denoted, respectively, with up and down arrows inside rounded squares. Lastly, the function blocks apply either a sparsity operation or an exponential-function operation to the quantities on the given path; the corresponding parameter values for these operations are offset from these blocks. We omit showing the actual optimization process but note that the feed-forward connections are largely devoted to computing gradients of the two cost functions, $\nabla_{\gamma_{i,t}} \mathcal{L}_1$ and $\nabla_{\kappa_{i,t}} \mathcal{L}_2$, that are used to update the states $\gamma_{i,t}$ and causes $\kappa_{i,t}$.

2.1 Network Formulation

Our ADPCNs consist of two stages at each layer, which are outlined in fig. 1. The first stage entails inferring the hidden states, which essentially are a feature-based representation used to describe the stimuli. States are formed, at the first layer, via sparse coding in conjunction with a temporal-state-space model to map the stimuli to an over-complete dictionary of convolutional filters. Subsequent DPCN layers follow the same process, with the only change being that the hidden causes assume the role of the observed stimuli.

We define state inference via a least-absolute-shrinkage-and-selection-operator (LASSO) cost. We present this, here, for the case of single-channel stimuli. The extension to multiple channels is straightforward.

Definition 2. Let $\gamma_{i,t} \in \mathbb{R}_+^{k_i}$ be the hidden states at time t and at model layer i . Let $C_i \in \mathbb{R}^{k_i \times k_i}$ be a hidden-state-transition matrix. Let $D_i^T \in \mathbb{R}^{k_i \times k_{i-1}}$ be a Toeplitz-form matrix with $q_i \in \mathbb{R}_+$ filters structured as in [28]. The state-inference cost function to be minimized, with respect to $\gamma_{i,t}$, C_i , and D_i^T , is given by

$$\mathcal{L}_1(\gamma_{i,t}, \kappa_{i,t}, C_i, D_i^T; \alpha_i, \lambda_{i,t}) = \frac{1}{2} \left(\|\kappa_{i-1,t} - D_i^T \gamma_{i,t}\|_2^2 + \alpha_i \|\gamma_{i,t} - C_i \gamma_{i,t-1}\|_1 + \sum_{k'=1}^{k_i} [\lambda_{i,t}]_{k'} |\gamma_{i,t}]_{k'} \right),$$

where $\kappa_{0,t} = y_t$. The first term in this cost quantifies the L_2 prediction error, $\epsilon'_{i,t} = \kappa_{i-1,t} - D_i^T \gamma_{i,t}$, at layer i . For the input layer, this error is $\epsilon_{1,t} = y_t - D_1^T \gamma_{1,t}$. In either case, the aim is to ensure that the local reconstruction error between layers is minimized. The second term constrains the next-state dynamics to be described by the state-transition matrix. For static stimuli, indexed by t , the state feed-back is replaced by $\kappa_{i,t} - D_{i+1,t}^T \gamma_{i+1,t}$. The strength of the recurrent feed-back connection is driven by $\alpha_i \in \mathbb{R}_+$. The transitions are L_1 -sparse to make the state-space representation consistent. Without such a norm penalty, the innovations would not be sparse due to the feed-back. The final term enforces L_1 -sparsity of the states, with the amount controlled by $\lambda_{i,t} \in \mathbb{R}_+^{k_i}$.

Proposition 1. Let $\gamma_{i,t} \in \mathbb{R}_+^{k_i}$ be the hidden states at time t and at model layer i . Let $D_i^T \in \mathbb{R}^{k_i \times k_{i-1}}$ be a Toeplitz-form matrix of $q_i \in \mathbb{R}_+$ filters. The matrix-vector multiplication $D_i^T \gamma_{i,t}$ is functionally equivalent to convolution for all layers i .

When projected back into the original visual space of the input, the dictionaries define a series of receptive fields. The hidden states, at least for the initial layers of the hierarchy thus act as basic feature detectors. They often resemble the simple cells in the visual cortex [29].

Ideally, we would prefer L_0 -sparsity to the L_1 variant used in the state-inference cost, as it does not impose shrinkage on the hidden-state values. However, by sacrificing this property, we gain cost convexity, which aids in efficient numerical optimization with provable convergence.

Proposition 2. Let $\gamma_{i,t} \in \mathbb{R}_+^{k_i}$ be the hidden states at time t and at model layer i . Let $C_i \in \mathbb{R}^{k_i \times k_i}$ be a hidden-state-transition matrix. Let $D_i^T \in \mathbb{R}^{k_i \times k_{i-1}}$ be a Toeplitz-form matrix with $q_i \in \mathbb{R}_+$ filters. For $\alpha_i, \lambda_{i,t} \in \mathbb{R}_+$, the hidden state cost function $\mathcal{L}_1(\gamma_{i,t}, \kappa_{i,t}, C_i, D_i^T; \alpha_i, \lambda_{i,t})$ is convex.

The state-based feature representations constructed by the first stage are not guaranteed to be invariant to various transforms. Discrimination can be impeded, as a result. The second DPCN processing stage thus entails explicitly imposing this behavior. Local translation invariance is attained by leveraging the spatial relationships of the states in neighborhoods via the sum-pooling of states. Invariance to more complex transformations, like rotation and spatial frequency, is made possible through the inference of subsequent hidden causes.

Sparse cause inference is driven by a LASSO-based cost that captures non-linear dependencies between components in the pooled states.

Definition 3. Let $\gamma_{i,t} \in \mathbb{R}_+^{k_i}$ be the hidden states and $\kappa_{i,t} \in \mathbb{R}^{d_i}$ be the bottom-up hidden causes at time t and model layer i . Let $\kappa'_{i,t} \in \mathbb{R}^{d_i}$ be the top-down-inferred causes. Let $C_i \in \mathbb{R}^{k \times k}$ be a hidden-state-transition matrix. Let $D_i^\top \in \mathbb{R}^{k_i \times k_{i-1}}$ be a Toeplitz-form matrix of $q_i \in \mathbb{R}_+$ filters. Let $G_i \in \mathbb{R}^{d_i \times k_i}$ be an invariant matrix. The hidden-cause cost to be minimized, with respect to $\kappa_{i,t}$ and G_i , is given by

$$\mathcal{L}_2(\gamma_{i,t}, \kappa_{i,t}, G_i; \alpha'_i, \lambda'_i, \eta'_i, \lambda_{i,t}) = \frac{1}{2} \left(\left(\sum_{j=1}^n \sum_{k'=1}^{k_i} |[\lambda_{i,t}]_{k'} \gamma_{i,t}^j| \right) + \eta'_i \|\kappa_{i,t} - \kappa'_{i,t}\|_2^2 + \lambda'_i \|\kappa_{i,t}\|_1 \right),$$

where $\lambda_{i,t,k'} = \alpha'_i (1 + \exp(-[G_i \kappa_{i,t}]_k))$, $\alpha'_i \in \mathbb{R}_+$. The first term in this cost models the multiplicative interaction of the causes $\kappa_{i,t}$ with the sum-pooled states $\gamma_{i,t}^j$ through an invariant matrix $G_i \in \mathbb{R}^{d_i \times k_i}$. This characterizes the shape of the sparse prior on the states. That is, the invariant matrix is adapted such that each component of the causes are connected to element groups in the accumulated states that co-occur frequently. Co-occurring components typically share common statistical regularities, thereby yielding locally invariant representations [30]. The second term specifies that the difference between the bottom-up $\kappa_{i,t}$ and top-down inferred causes $\kappa'_{i,t}$ should be small, with the term weight specified by $\eta'_i \in \mathbb{R}_+$. The final term imposes L_1 sparsity, with the amount controlled by $\lambda'_i \in \mathbb{R}_+$, to prevent the intermediate representations from being dense.

The causes obtained by solving the above LASSO cost will behave somewhat like complex cells in the visual cortex [31]. Similar results are found in temporally coherent networks [32], albeit without guaranteed feature invariance.

As with the state-inference cost, we employ L_1 sparsity in the hidden-cause cost for practical reasons, even though we would prefer L_0 sparsity for its theoretical appeal.

Proposition 3. Let $\gamma_{i,t} \in \mathbb{R}_+^{k_i}$ be the hidden states and $\kappa_{i,t} \in \mathbb{R}^{d_i}$ be the hidden causes at time t and model layer i . Let $C_i \in \mathbb{R}^{k_i \times k_i}$ be a hidden-state-transition matrix, $D_i^\top \in \mathbb{R}_+^{k_i \times k_{i-1}}$ be a Toeplitz-form matrix of filters, and $G_i \in \mathbb{R}^{d_i \times k_i}$ be an invariant matrix. For $\alpha'_i, \lambda'_i, \eta'_i \in \mathbb{R}_+$ and $\lambda_{i,t} \in \mathbb{R}_+^{k_i}$, the hidden cause cost function $\mathcal{L}_2(\gamma_{i,t}, \kappa_{i,t}, G_i; \alpha'_i, \lambda'_i, \eta'_i, \lambda_{i,t})$ is convex.

Defining states and causes as we have specified above has significant advantages. DPCNs are, for instance, incredibly parameter efficient compared to standard recurrent-convolutional autoencoders. Often, few filters are needed to adequately synthesize an observed stimuli under varying conditions, which is a byproduct of the explicit feature invariance imposed by the non-linear, sparse cause inference.

2.2 Network Inference

The propagation and transformation of observed stimuli in a DPCN is more involved than for standard network architectures. At any layer in the ADPCN, the hidden, sparse states and unknown, sparse causes that minimize the two-part LASSO cost must be inferred to create the feed-forward observations for the next DPCN layer.

Joint inference of the states and causes can be done in a manner similar to block coordinate descent. That is, for a given mini-batch of stimuli, the states can be updated by solving the corresponding LASSO cost while holding the causes fixed. The causes can then be updated while holding the states fixed. Altering either of these representations amounts to solving a convolutional, L_1 -sparse-coding problem. The presence of discontinuous, L_1 -based terms in the LASSO costs complicates the application of standard optimization techniques, though.

Here, we consider a fast proximal-gradient-based approach for separating and accounting for the smooth and non-smooth components of the LASSO costs. This approach is motivated and analyzed in the appendix.

Definition 4. Let $\gamma_{i,t} \in \mathbb{R}_+^{k_i}$ be the hidden states and $\pi_{i,t} \in \mathbb{R}_+^{k_i}$ be the auxiliary hidden states at time t and model layer i . These auxiliary hidden states will be linear combinations of hidden states across different times. Let $C_i \in \mathbb{R}^{k_i \times k_i}$ be a hidden-state-transition matrix. As well, let $D_i^\top \in \mathbb{R}^{k_i \times k_{i-1}}$ be a Toeplitz-form matrix of $q_i \in \mathbb{R}_+$ filters. For an inertial sequence $\beta_m \in \mathbb{R}_+$ and an adjustable step size $\tau_{i,t}^m \in \mathbb{R}_+$, the hidden-state inference process, indexed by iteration m , is given by the following expressions

$$\gamma_{i,t+1}^m = \text{PROX}_{\lambda_{i,t}} \left(\pi_{i,t}^m - \lambda_{i,t} \tau_{i,t}^m \nabla_{\pi_{i,t}^m} \mathcal{L}_1(\pi_{i,t}^m, \kappa_{i,t}, C_i, D_i^\top; \alpha_i, \lambda_{i,t}) \right), \quad \pi_{i,t}^{m+1} = \gamma_{i,t+1}^m + \beta_m (\gamma_{i,t+1}^m - \gamma_{i,t+1}^{m-1})$$

with $\mathcal{L}_1(\pi_{i,t}^m, \kappa_{i,t}, C_i, D_i^\top; \alpha_i, \lambda_{i,t}) = D_i^\top (\kappa_{i-1,t} - D_i \pi_{i,t}^m) + \alpha_i \Omega_i(\pi_{i,t}^m)$. Here, use a Nesterov smoothing, $\Omega_i(\pi_{i,t}^m) = \arg \max_{\|\Omega_{i,t}\|_\infty \leq 1} \Omega_{i,t}^\top (\pi_{i,t}^m - C_i \pi_{i,t}^{m-1})$, $\Omega_{i,t} \in \mathbb{R}^{k_i}$, to approximate the non-smooth state transition. Small values for the hidden states are clamped via a soft thresholding function implicit to the proximal operator, which leads to a sparse solution. The states are then spatially max pooled over local neighborhoods, using non-overlapping windows, to reduce their resolution, $\gamma_{i,t+1} = \text{POOL}(\gamma_{i,t+1})$.

Definition 5. Let $\gamma_{i,t} \in \mathbb{R}_+^{k_i}$ be the hidden states and $\kappa_{i,t} \in \mathbb{R}^{d_i}$ be the hidden causes at time t and model layer i . Let $C_i \in \mathbb{R}^{k_i \times k_i}$ be a hidden-state-transition matrix, $D_i^\top \in \mathbb{R}^{k_i \times k_{i-1}}$ be a Toeplitz-form matrix of $q_i \in \mathbb{R}_+$

filters, and $G_i \in \mathbb{R}^{d_i \times k_i}$ be an invariant matrix. For an adjustable step size $\tau'_{i,t} \in \mathbb{R}_+$ and inertial sequence $\beta'_m \in \mathbb{R}_+$, the hidden-cause inference process, indexed by m , is given by the following expressions

$$\kappa'_{i,t+1} = \text{PROX}_{\lambda'_i} \left(\pi'_{i,t} - \lambda'_i \tau'_{i,t} \nabla_{\pi'_{i,t}} \mathcal{L}_2(\gamma_{i,t+1}, \pi'_{i,t}, G_i; \alpha'_i, \lambda'_i, \eta'_i, \lambda_{i,t}) \right), \quad \pi'_{i,t}^{m+1} = \kappa'_{i,t+1} + \beta'_m (\kappa'_{i,t+1} - \kappa'_{i,t+1}^{m-1})$$

with $\nabla_{\pi'_{i,t}} \mathcal{L}_2(\gamma_{i,t+1}, \pi'_{i,t}, G_i; \alpha'_i, \lambda'_i, \eta'_i, \lambda_{i,t}) = -\alpha'_i G_i^\top \exp(-G_i \pi'_{i,t}) |\gamma_{i,t+1}^j| + 2\eta'_i (\kappa'_{i,t+1} - \kappa'_{i,t})$. Small values for the hidden causes are clamped via an implicit soft thresholding function, which leads to a sparse solution. The inferred causes are then used to update the sparsity parameter $\lambda_{i,t+1} = \alpha'_i (1 + \exp(-\text{UNPOOL}(G_i \kappa'_{i,t+1})))$ using spatial max unpooling.

In both cases, the step size is bounded by the Lipschitz constant of the LASSO cost to be solved. The choice of the inertial sequence greatly affects the convergence properties of the optimization.

Proposition 4. Let $\gamma_{i,t} \in \mathbb{R}_+^{k_i}$ be the hidden states and $\kappa_{i,t} \in \mathbb{R}^{d_i}$ be the hidden causes. The state iterates $\{\gamma_{i,t+1}^m\}_{m=1}^\infty$ strongly converge to the global solution of $\mathcal{L}_1(\gamma_{i,t}, \kappa_{i,t}, C_i, D_i^\top; \alpha_i, \lambda_{i,t})$ for the accelerated proximal gradient scheme. Likewise, the cause iterates $\{\kappa'_{i,t+1}^m\}_{m=1}^\infty$ for the accelerated proximal gradient scheme strongly converge to the global solution of $\mathcal{L}_2(\gamma_{i,t+1}, \kappa_{i,t}, G_i; \alpha'_i, \lambda'_i, \eta'_i, \lambda_{i,t})$ at a sub-polynomial rate. This occurs when using the inertial sequences $\beta_m, \beta'_m = (k_m - 1)/k_{m+1}$, where k_m depends polynomially on m .

In this bottom-up inference process, there is an implicit assumption that the top-down predictions of the causes are available. This, however, is not the case for each iteration of a mini batch being propagated through the DPCN. We therefore consider an approximate, top-down prediction using the states from the previous time instance and, starting from the first layer, perform bottom-up inference using this prediction.

Definition 6. At the beginning of every time step t , using the state-space model at each layer, the likely top-down causes, $\kappa'_{i-1,t} \in \mathbb{R}^{d_{i-1}}$, are predicted using the previous states $\gamma_{i,t} \in \mathbb{R}^{k_i}$ and the causes $\kappa_{i,t} \in \mathbb{R}^{d_i}$. That is, for the filter dictionary matrix, the following top-down update is performed

$$\kappa'_{i-1,t} = D_i^\top \gamma'_{i,t}, \quad \gamma'_{i,t} = \arg \min_{\gamma_{i,t}} \left(\lambda'_i \|\gamma_{i,t+1} - C_i \gamma_{i,t}\|_1 + \alpha'_i \|\gamma_{i,t}\|_1 \left(1 + \exp(-\text{unpool}(G_i \kappa_{i,t})) \right) \right),$$

except for the last layer, wherein $\kappa'_{i,t+1} = \kappa_{i,t}$. This minimization problem has an algebraic expression for the global solution: $[\gamma'_{i,t}]_k = [C_{i,t} \gamma_{i,t-1}]_k$, whenever $\alpha'_i \lambda_{i,t,k} < \alpha_i$, and zero otherwise.

These top-down predictions serve an important role during inference, as they transfer abstract knowledge from higher layers into lower ones, thereby improving the overall representation quality. The predictions also modulate the representations due to state zeroing by the sparsity hyperparameter.

Alongside the state and cause inference is a learning process for fitting the ADPCN parameters to the stimuli. Here, we consider layer-wise, gradient-descent training without top-down information, which is performed once inference has stabilized for a given mini batch. An overview of this procedure, within the variable inference, is presented in the online appendix (see appendix A).

3. Simulation Results

We now assess the capability of our inference strategy for unsupervised ADPCNs. We focus on static visual stimuli (see section 3.1). We demonstrate that ADPCNs uncover stable, meaningful feature representation more quickly than DPCNs (see section 3.2). This permits ADPCNs to often exceed the performance of deep unsupervised and deep supervised networks.

3.1. Simulation Preliminaries

Data and Pre-processing. We relied on five datasets for our simulations. Two of these, MNIST and FMNIST, were of single-channel, static visual stimuli. The remaining three, CIFAR-10/100 and STL-10, contained multi-channel, static visual stimuli. We whitened each dataset and zeroed their means. We relied on the default training and test set definitions for each dataset.

Training and Inference Protocols. For learning the DPCN and ADPCN parameters, we relied on ADAM-based gradient descent with mini batches [33]. We set the initial learning rate to $\eta_0 = 10^{-3}$, which helped prevent overshooting the global optimum. The learning rate was decreased by half every epoch. We used exponential decay rates of 9.0×10^{-1} and 9.9×10^{-1} for the first- and second-order gradient moments in ADAM, respectively, which were employed to perform bias correction and adjust the per-parameter learning rates. An epsilon additive factor of 10^{-8} was used to preempt division by zero. We used an initial forgetting factor value of $\theta_0 = 0.7$. This factor was increased by a tenth every thousand mini batches to stabilize convergence. We considered a mini-batch size of 32 randomly selected samples to improve solution quality [34].

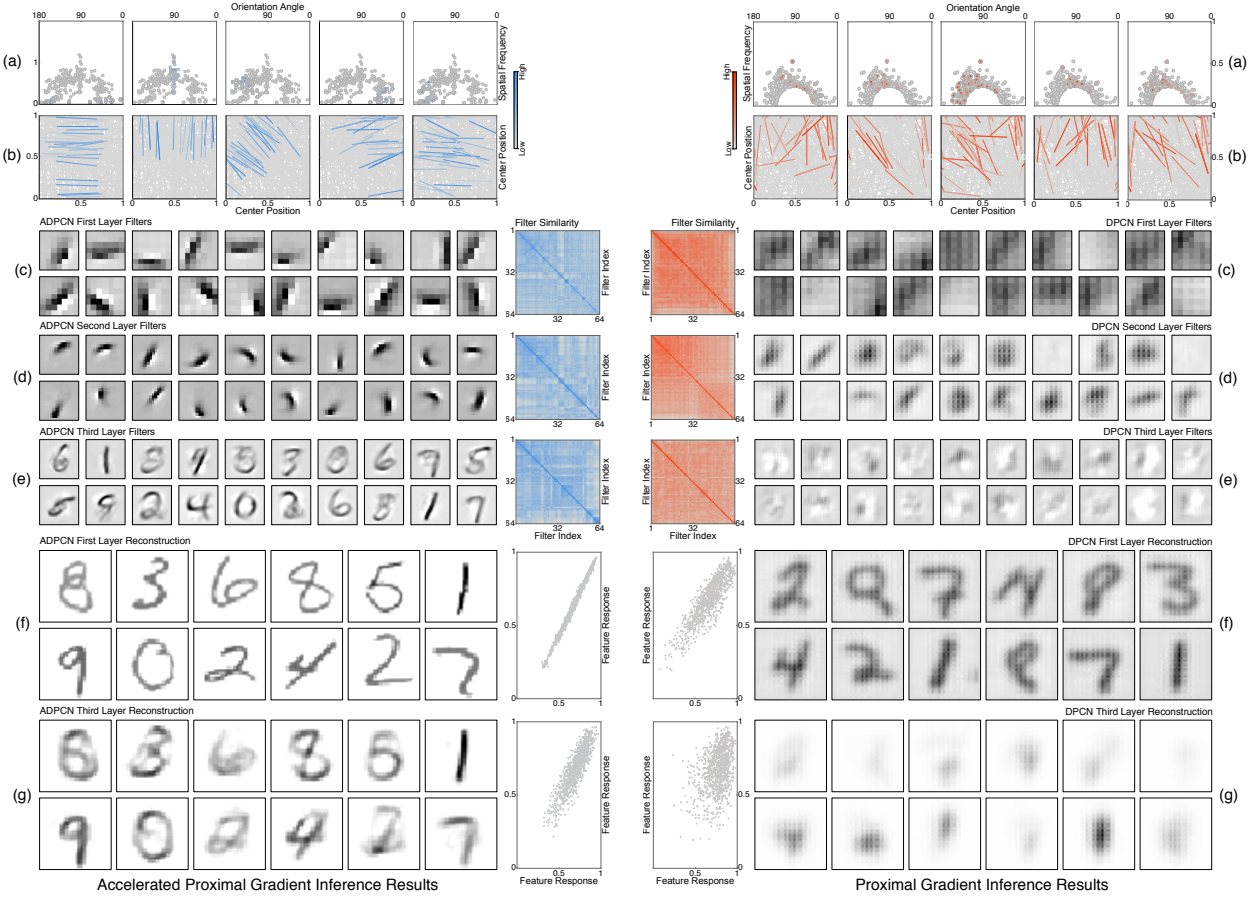


Figure 2: A comparison of accelerated proximal gradient inference and learning (left, blue) and proximal gradient inference and learning (right, red) the MNIST dataset. The presented results are shown after training with mini batches for two epochs. (a) Polar scatter plots of the orientation angles versus spatial frequency for the first-layer causes. (b) Line plots of the normalized center positions with included orientations for the first-layer causes. For both (a) and (b), we fit Gabor filters to the first-layer causes; locally optimal filter parameters were selected via a gradient-descent scheme. The plots are color-coded according to the connection strength between the invariance matrix and the observation matrix in the first network layer. Higher connection strengths indicate subsets of dictionary elements from the observation matrix that are most likely active when a column of the invariance matrix is also active. If a DPCN has been trained well, then the filters should have a small orientation-angle spread. Each plot represents a randomly chosen column of the first-layer invariance matrix. (c)–(e) Back-projected causes from the first, second, and third layers of the networks, respectively. Each plot represents a randomly chosen cause. The back-projected causes can be interpreted as receptive fields, with darker colors indicating a higher degree of activation. For each layer, we assess the filter similarity and provide VAT similarity plots. In these plots, low similarities are denoted using gray while higher similarities are denoted using progressively more vivid shades of either blue (accelerated proximal gradients) or red (proximal gradients). If a DPCN has been trained well, then there should be few to no duplicate filters. There, hence, should not be any conspicuous blocky structures along the main diagonal of the VAT similarity plots. (f)–(g) Reconstructed instances from a random batch at the first and third layer, respectively. For each layer, we also assess the feature similarity between the original training samples and the reconstructed versions and provide corresponding scatter plots. If a DPCN reconstructs the input samples well, then there should be a strong linear relationship between the features. Higher distributional spreads and shifts away from the main diagonal indicate larger reconstruction errors.

For DPCN and ADPCN inference, we relied on variable numbers of filters along with variable filter sizes, with the actual amounts determined by the specific stimuli dataset. We primarily set the sparsity parameters to $\lambda_1, \lambda'_1 = 0.2$, $\lambda_2, \lambda'_2 = 0.25$, and $\lambda_3, \lambda'_3 = 0.35$. Such values permitted retaining much of the visual content in the first two layers while compressing it more pronouncedly in the third. Some stimuli datasets have slightly altered parameter values. Due to the static nature of the stimuli, we did not have temporal state feed-back. We did, however, propagate the cause-state difference between layers and set the feed-back strengths, for most simulations, to $\alpha_1, \alpha_2 = 1$ and $\alpha_3 = 3$. The stronger feed-back amount in the third layer aided in suppressing noise without adversely impacting the in earlier layers priors. We fixed the causal sparsity constants to $\alpha'_1, \alpha'_2, \alpha'_3 = 1$. We terminated the accelerated and regular FISTA inference processes after 50 and 1000 iterations, respectively, per mini batch. A significantly lower number of iterations was used in the former case, since the chosen inertial sequence facilitated quick convergence.

3.2. Simulation Results and Discussions

Network Architecture. We considered the same architecture for the DPCNs and ADPCNs. At the first layer, we used 32 states with 7×7 filters and 64 causes with 7×7 filters; for the invariance results, we temporarily increased the states and causes to 128 and 256, respectively. At the second and third layers, we used 64 states and 256 states with 5×5 and 7×7 filters, respectively. We also used 128 and 1024 causes with 5×5 and 7×7 filters, respectively. We performed

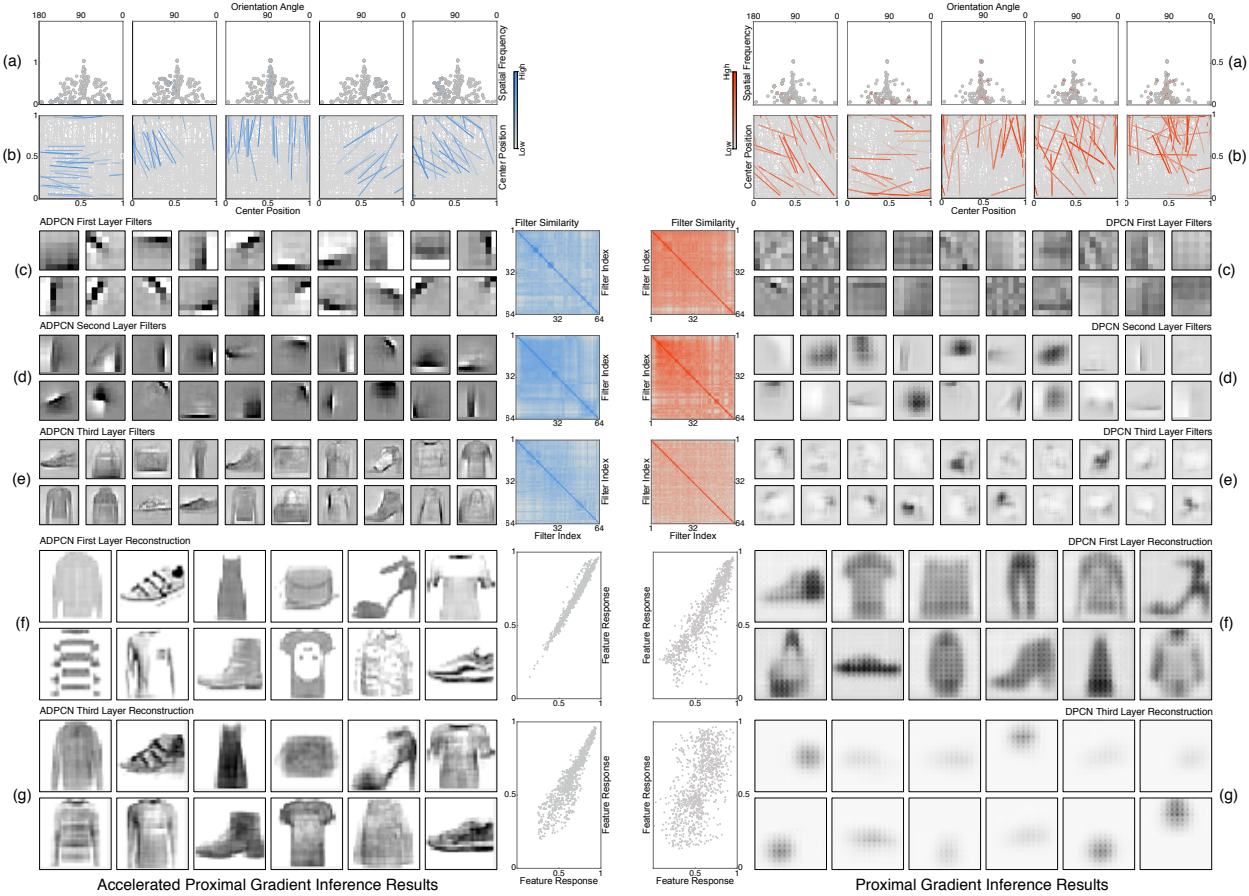


Figure 3: A comparison of accelerated proximal gradient inference and learning (left, blue) and proximal gradient inference and learning (right, red) the FMNIST dataset. The presented results are shown after training with mini batches for two epochs. See fig. 2 for descriptions of the plots.

2×2 max pooling between the states and the causes at each layer. In total, the networks had 72224 parameters for a majority of the simulations.

Simulation Results. Simulation findings are presented in fig. 2 and fig. 3 for the single-channel MNIST and FMNIST datasets, respectively. Findings for the multi-channel CIFAR-10/100 and STL-10 datasets are, respectively, shown in fig. 4 and fig. 5. The results for both ADPCNs and DPCNs were for after two epochs.

For these datasets, the ADPCNs were successful in quickly uncovering invariant representations. Most of the columns in the invariance matrix grouped together dictionary elements that had very similar orientation and frequency while being insensitive to translation (see fig. 2(a) to fig. 5(a)). Likewise, for each active invariance-matrix column, a subset of the dictionary elements were grouped together by orientation and spatial position, which indicated invariance to other properties like spatial frequency and center position (see fig. 2(b) to fig. 5(b)). The DPCNs, in comparison, had representations that would be significantly altered by transformations other than translation. This occurred because subsets of the dictionary elements were not grouped according to various characteristics. Discrimination performance hence suffered for stimuli samples that were slightly altered.

As well, the ADPCNs learned meaningful filters from the stimuli. The first two layers of our ADPCNs had causal receptive fields that mimicked the behavior of simple and complex cells in the primate vision system (see fig. 2(c)–(d) to fig. 5(c)–(d)). The fields for the first layer were predominantly divided into two types: low-frequency and high-frequency, localized band-pass filters. The former mainly encoded regions of uniform intensity and color along with slowly varying texture. The latter described contours and hence sharp boundaries. Such filters permitted accurately reconstructing the input stimuli (see fig. 2(f) to fig. 5(f)). The second-layer receptive fields were non-linear combinations of those in the first that became activated by more complicated visual patterns, such as curves and junctions. A similar division of receptive fields into two categories was encountered in the second ADPCN layer. More filters were activated by contours, however, than in the first layer. For both layers, the filters were mostly unique, which is captured in the ordered similarity plots (see fig. 2(c)–(d) to fig. 5(c)–(d)). Beyond two layers, the ADPCN receptive fields encompassed entire objects (see fig. 2(e) to fig. 5(e)). They were, however, average representations, not highly specific ones, due to the limited number of causes (see fig. 2(g) to fig. 5(g)). The backgrounds in the visual stimuli were often suppressed at this layer, which greatly enhanced performance. The ordered similarity plots indicate that none of the third-layer filters appeared to be duplicated for either dataset. This trend also held for the first- and

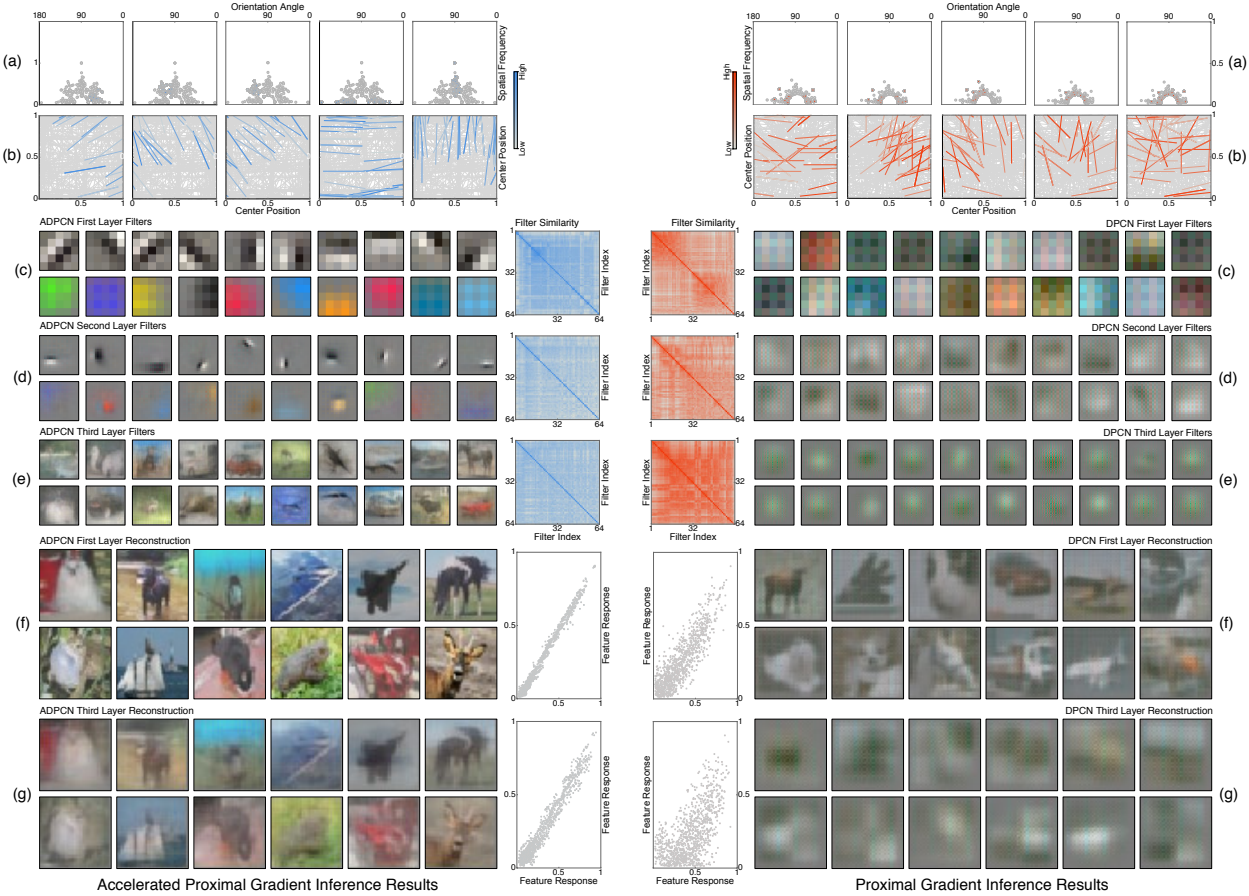


Figure 4: A comparison of accelerated proximal gradient inference and learning (left, blue) and proximal gradient inference and learning (right, red) on the CIFAR-10/100 datasets. The presented results are shown after training with mini batches for two epochs. See fig. 2 for descriptions of the plots.

second-layer receptive fields, implying that the ADPCNs emphasized the extraction of non-redundant features.

DPCNs, in contrast, did not stabilize to viable receptive fields at the same rate as the ADPCNs (see fig. 2(c)–(d) to fig. 5(c)–(d)). For MNIST, the first-layer DPCN receptive fields had some localized band-pass structure that was similar to Gabor filters. The overall spread of the fields made it difficult to accurately detect abrupt transitions and hence recreate the input stimuli, though. The reconstructions thus were heavily distorted and blurred (see fig. 2(f)). For FMNIST, the first-layer receptive fields focused on either low-frequency details, such as either constant grayscale values or slow-changing grayscale gradients, or higher-frequency details, such as periodic texture. While some of the causes became specialized band-pass-like filters, there were not enough to adequately preserve sharp edges. The stimuli reconstructions were thus also distorted, with much of the high-frequency content completely removed (see fig. 3(f)). Similar results were encountered for CIFAR-10/100 and STL-10 (see fig. 4(f) to fig. 5). For all of the datasets, the second-layer receptive fields became even less organized than in the first layer. They were mostly activated by blob-like visual patterns, which did not preserve enough visual content for recreating a close resemblance of the input stimuli beyond the first layer. The DPCNs were unable to learn relevant representations in the third layer, as a consequence. The receptive fields for this network layer were unique, by virtue of being essentially random, but were largely useless in extracting stimuli-specific details (see fig. 2(e) to fig. 5(e)). This further degraded the reconstruction quality to where the inputs were unrecognizable (see fig. 2(g) to fig. 5(g)). Discrimination was adversely impacted due to this severe lack of identifying characteristics. The filter redundancy also impacted performance, as there was not enough unique information to be back-propagated to earlier layers to inform the choice of better receptive fields.

Overall, the layer-aggregated ADPCN features yielded high-performing unsupervised classifiers (see appendix B). They achieved state-of-the-art unsupervised recognition rates for each dataset. They also were on par with deep networks trained in a supervised fashion, despite having orders of magnitude fewer parameters. Although the features from all layers had a positive net contribution, those from the third layer yielded the largest performance boost. The DPCNs exhibited poor performance, in comparison. Only the first-layer features aided classification. The remainder largely worsened the recognition capabilities. For both the DPCNs and ADPCNs, we relied on a five-nearest neighbor classifier with an unsupervised-learned metric distance [35] to label the stimuli samples.

Simulation Discussions. Our simulations indicate that ADPCNs were more effective at uncovering highly discriminative feature representations of visual stimuli than the original DPCN inference strategy. A trait that con-

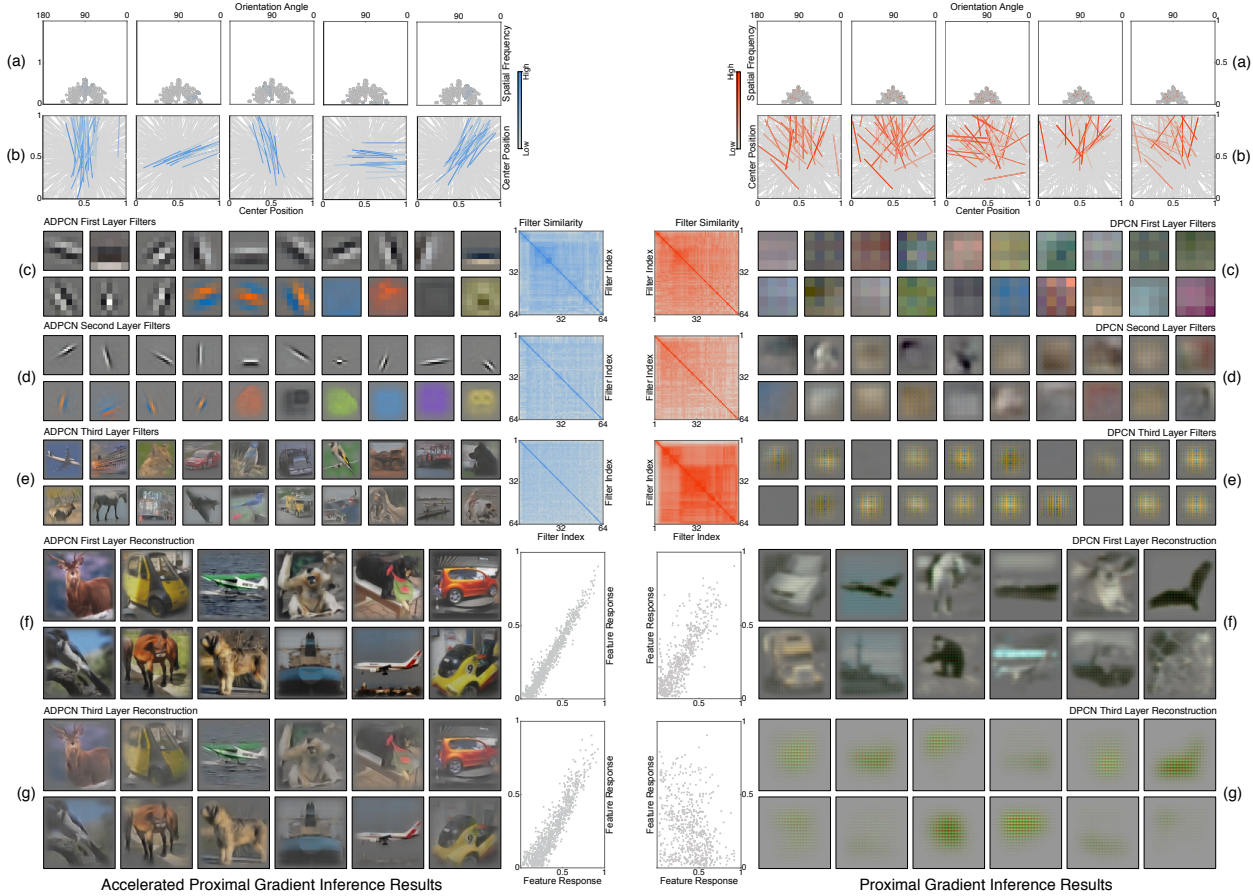


Figure 5: A comparison of accelerated proximal gradient inference and learning (left, blue) and proximal gradient inference and learning (right, red) the STL-10 dataset. The presented results are shown after training with mini batches for two epochs. See fig. 2 for descriptions of the plots.

tributed greatly to the ADPCNs' success was its significantly improved search rate.

As noted in the appendix, proximal-gradient-type schemes can undergo four separate search phases, some of which have different local convergence rates. In one of the phases, the constant-step regime, both the states and causes underwent rapid improvements. However, in two phases, the local convergence rate was slow whenever the largest eigenvalue of a certain recurrence matrix was less than the current inertial-sequence magnitude. For linear inertial sequences, like those found in the proximal-gradient-based DPCNs, this condition occurred early during the optimization process. That is, for such sequences, the growth was initially very rapid and followed a logarithmic rate. Within just a few iterations, the sequence magnitude had exceeded the eigenvalue, which preempted the fast constant-step regime. The rate of convergence became worse than sublinear. A large number of search steps was thus needed to move toward the global solution. However, when this happened, the total number of proximal-gradient iterations had been reached and the search was terminated. The search was, alternatively, stopped early due to a lack of progress across consecutive iterations. In either case, the states and causes did not adequately stabilize for a given mini batch. The poor state and cause representations, naturally, were integrated into the filter dictionary matrices and invariant matrices during the learning updates, which disrupted the priors in the early hierarchy for future stimuli. The convergence was further stymied by cost rippling; proximal-gradient-based optimization thus did not behave like a pure descent method in two out of the four phases. Such behavior was caused by the eigenvalues of another recurrence matrix being a pair of complex conjugates, which necessitated oscillating between the two. All of these factors made it difficult to propagate meaningful bottom-up information [36] beyond the first layer. The top-down details from higher layers were hence ineffective at modifying the priors to disambiguate the stimuli [37].

The ADPCNs largely avoided these issues. After the constant-step regime, the search switched to one of two potentially slower phases. However, the APDCNs' inertial-sequence growth rate was rather muted, as opposed to that of the DPCNs. The chance of exceeding the largest eigenvalue of the augmented, auxiliary-variable recurrence matrix was low for the ADPCNs. The search thus could proceed unhindered toward the global solution. Moreover, since the eigenvalue-magnitude threshold was often not reached, the largest eigenvalue of the augmented, mapping recurrence matrix was real-valued, not complex. This meant that the accelerated proximal gradients would behave like a descent method; it thus would not experience localized cost rippling due to alternating between conjugate pairs. Both properties promoted rapid stabilization of the states and causes, which expedited the formation of beneficial priors

throughout much of the early-layer network inference. These priors facilitated the construction of transformation-insensitive feature abstractions in deeper network layers, due to the bottom-up forwarding of stimuli-relevant signals. The recurrent, top-down connections, in turn, suitably altered the representation sparsity, thereby ignoring extraneous details that did not contribute greatly to the reconstruction quality. This would bias in favor of valuable stimuli, which is analogous to observed functionality in the frontal and parietal cortices [38]. The descending pathways also carried predictive responses, in the form of templates of expected stimuli that would be matched to the current and future mini batches to aid recognition [39]. That is, the templates conveyed contextual information for extracting task-specific information, which made recognition more reliable [40, 41].

There were other traits that contributed to the success of the ADPCNs. For instance, the first-layer receptive fields were largely similar to that of simple cells in the primary visual cortex. Simple cells often implement Gabor-like filters with generic preferred stimuli that correspond to oriented edges [42, 43]. Such filters were highly useful within the ADPCNs, since relations between activations for specific spatial locations tended to be distinctive between objects in visual stimuli. Activations were also obtained, in a Gabor space, that facilitated the construction of naturally sparse representations and could then be hierarchically extended, which was what we ultimately sought in the ADPCNs. Changes in object location, scale, and orientation could be reliably detected, within this Gabor space, thereby aiding in the creation of transformation-invariant features that also permitted near-perfect stimuli reconstructions at the first layer. The uniqueness of the band-pass filters was beneficial, as it permitted the ADPCNs to fixate on non-redundant stimuli characteristics. How these filters arose and the rate at which they formed were also important aspects that aided in the ADPCNs' success. They emerged due to feed-back from high-level visual network areas, which quickly reduced activity in lower areas to simplify the description of the stimuli to some of its most basic elements [44]. In doing so, alternate explanations were suppressed, and only the most dominant, fundamental causes of the stimuli remained [3], which were oriented luminance contours. This rapid stabilization of filters was exactly functionality that we would expect to encounter in an efficient predictive coding process. It was hence well aligned with contemporary neurophysiological theory [45].

Beyond the first layer, the ADPCNs exhibited an increase in specificity, abstraction, and invariance for deeper hierarchies [46], which aligned well with the current understanding of the vision system [47]. This also aided in the ADPCNs' success. The second-layer receptive fields, in the case of MNIST, became sensitive to curved sub-strokes for the hand-written digits, which is similar to prestriate cortex functionality [48]. For FMNIST, they emphasized abrupt transitions found in regions of the apparel and fashion accessories. This mimics aspects of shape-pattern-selectivity behaviors found in the extrastriate cortices [49, 50]. For STL-10, the receptive fields were often elongated Gabor-like filters, which can be found in the prestriate cortex [51]. All of these features systematically focused on object-relevant visual details, thereby aiding recognition. At the deepest layer, the receptive fields were entirely object specific, which is functionality somewhat akin to the neurons in the primate infero-temporal cortex [52]. It is also related to memory activity [53, 54]. The representations were additionally translation and rotation insensitive, similar to inferotemporal cortex neurons [55–57], and changed little with respect to scale and spatial-frequency changes, similar to neurons in the middle temporal area [58, 59]. To our knowledge, such invariant, whole-object sensitivity within a single layer has not been witnessed in any existing predictive-coding model. Based on contemporary theories [60], we believe that the receptive-field feed-back from the final layer contributed to the effective connectivity in the earlier network layers [61]. That is, the role of this final layer was to disambiguate local image components by creating a template that was fed back, which then selectively enhanced object components and suppressed interfering background components [62]. This biologically plausible behavior was crucial for achieving high discrimination rates on CIFAR-10/100 and STL-10, since the objects of interest were scattered amongst cluttered scenes.

4. Conclusions

Here, we have revisited the problem of unsupervised predictive coding. We considered a hierarchical, generative network, the ADPCN, for reconstructing observed stimuli. This network was composed of temporal sparse-coding models with bi-directional connectivity. The interaction of the information passed by top-down and bottom-up connections across the models permitted the extraction of invariant, increasingly abstract feature representations.

Our contribution in this paper was an effective means of inferring the underlying components of the feature representations, which are the sparse states and causes. Previously, a proximal-gradient-type approach was used for this purpose. Despite its promising theoretical guarantees, though, it exhibited poor empirical performance. This practically limited the number of layered models that could be considered in the DPCNs. It also extensively curtailed the quality of the stimuli features that could be extracted. Here, we considered a parallelizable, vastly accelerated proximal-gradient strategy that overcame these issues. It allowed us to go beyond the existing two-layer limitation, facilitating the construction of arbitrary-layered DPCNs. Each layer led to increasingly enhanced performance for object analysis, as the information from higher layers was propagated to earlier ones to form more effective stimuli priors for bottom-up processing. Most crucially, our optimization strategy immensely streamlined inference.

Often, only one or two presentations of the stimuli was necessary to reach a stable filter dictionary, and hence a corresponding set of sparse states and sparse causes, with good object analysis performance. The previous optimization approach required many times more presentations before a stable set of filters was uncovered. The resulting features were also not nearly as discriminative as those from our proposed strategy.

We applied our ADPCNs to static-image datasets. For MNIST and FMNIST, the ADPCNs learned initial-layer receptive fields that mimicked aspects of the early stages of the primate vision system. The later network stages implemented receptive fields that encompassed entire objects. In the case of MNIST, the back-projected filters became pseudo averages of the hand-written numerical digits. Predominant writing styles were modeled well. For FMNIST, the back-projected filters were the various types of clothing and personal articles. General styles and some nuances were captured. To our knowledge, this is the first time that such object-scale receptive fields have been learned for predictive coding. This behavior helped yield unsupervised classifiers that achieved state-of-the-art performance. Such classifiers also outperformed supervised-trained deep networks, which lent credence to the complicated feature inference and invariance process that we employed. Similar results were witnessed for more complex natural-image datasets, such as CIFAR-10/100. The later-layer receptive fields again encompassed entire object categories. This yielded promising features that achieved state-of-the-art generalization performance compared to supervised-trained deep networks. This was despite our use of simple nearest-neighbor classifiers. It was also despite the fact that our ADPCNs had many times fewer convolutional filters than these other deep networks.

Our ADPCNs are readily applicable to video processing, much like the original DPCNs. This is because the ADPCNs implement a recurrent state-space model. For video modalities, the ADPCN performance may be even better than for static images, as the top-down, feed-back connections impose temporal constraints on the learning process. We will investigate this in our future research.

References

- [1] R. P. N. Rao and D. H. Ballard, "Predictive coding in the visual cortex: A functional interpretation of some extra-classical receptive-field effects," *Nature Neuroscience*, vol. 2, no. 1, pp. 79–87, 1999. Available: <http://dx.doi.org/10.1038/4580>
- [2] K. J. Friston and S. Kiebel, "Predictive coding under the free energy principle," *Philosophical Transactions of the Royal Society B*, vol. 364, no. 1521, pp. 1211–1221, 2009. Available: <http://dx.doi.org/10.1098/rstb.2008.0300>
- [3] M. W. Spratling, "Unsupervised learning of generative and discriminative weights encoding elementary image components in a predictive coding model of cortical functions," *Neural Computation*, vol. 24, no. 1, pp. 60–103, 2011. Available: http://dx.doi.org/10.1162/NECO_a_00222
- [4] K. J. Friston, "Hierarchical models of the brain," *PLOS Computational Biology*, vol. 4, no. 11, pp. e1000211(1–24), 2008. Available: <http://dx.doi.org/10.1371/journal.pcbi.1000211>
- [5] T. Hosoya, S. A. Baccus, and M. Meister, "Dynamic predictive coding by the retina," *Nature*, vol. 436, no. 7047, pp. 71–77, 2005. Available: <http://dx.doi.org/10.1038/nature03689>
- [6] R. Aukstulewicz and K. J. Friston, "Repetition suppression and its contextual determinants in predictive coding," *Cortex*, vol. 80, no. 1, pp. 125–140, 2016. Available: <http://dx.doi.org/10.1016/j.cortex.2015.11.024>
- [7] M. V. Srinivasan, S. B. Laughlin, and A. Dubs, "Predictive coding: A fresh view of inhibition in the retina," *Proceedings of the Royal Society B: Biological Sciences*, vol. 216, no. 1205, pp. 427–459, 1982. Available: <http://dx.doi.org/10.1098/rspb.1982.0085>
- [8] J. F. M. Jehee, C. Rothkopf, J. M. Beck, and D. H. Ballard, "Learning receptive fields using predictive feedback," *Journal of Physiology*, vol. 100, no. 1-3, pp. 125–132, 2006. Available: <http://dx.doi.org/10.1016/j.jphysparis.2006.09.011>
- [9] R. Chalasani and J. C. Principe, "Deep predictive coding networks," in *Proceedings of the International Conference on Learning Representations (ICLR)*, Scottsdale, AZ, USA, May 2-4 2013, pp. 1–13. Available: <https://arxiv.org/abs/1301.3541>
- [10] J. C. Principe and R. Chalasani, "Cognitive architectures for sensory processing," *Proceedings of the IEEE*, vol. 102, no. 4, pp. 514–525, 2014. Available: <http://dx.doi.org/10.1109/JPROC.2014.2307023>
- [11] R. Chalasani and J. C. Principe, "Context dependent encoding using convolutional dynamic networks," *IEEE Transactions on Neural Networks and Learning Systems*, vol. 26, no. 9, pp. 1992–2004, 2015. Available: <http://dx.doi.org/10.1109/TNNLS.2014.2360060>
- [12] W. Lotter, G. Kreiman, and D. Cox, "Deep predictive coding networks for video prediction and unsupervised learning," in *Proceedings of the International Conference on Learning Representations (ICLR)*, Toulon, France, April 24-26 2017, pp. 1–13. Available: <https://arxiv.org/abs/1605.08104>
- [13] K. Han, H. Wen, Y. Zhang, D. Fu, E. Culurciello, and Z. Liu, "Deep predictive coding network with locally recurrent processing for object recognition," in *Advances in Neural Information Processing Systems (NIPS)*, S. Bengio, H. Wallach, H. Larochelle, K. Grauman, N. Cesa-Bianchi, and R. Garnett, Eds. Red Hook, NY, USA: Curran Associates, 2018, pp. 9201–9213.
- [14] K. J. Friston, J. Kilner, and L. Harrison, "A free energy principle for the brain," *Journal of Physiology*, vol. 100, no. 1-3, pp. 70–87, 2006. Available: <http://dx.doi.org/10.1016/j.jphysparis.2006.10.001>
- [15] P. Földiák, "Learning invariance from transformation sequences," *Neural Computation*, vol. 3, no. 2, pp. 194–200, 1991. Available: <http://dx.doi.org/10.1162/neco.1991.3.2.194>
- [16] A. Hyvärinen and P. O. Hoyer, "A two-layer sparse coding model learns simple and complex cell receptive fields and topography from natural images," *Vision Research*, vol. 41, no. 18, pp. 2413–2423, 2001. Available: [http://dx.doi.org/10.1016/S0042-6989\(01\)00114-6](http://dx.doi.org/10.1016/S0042-6989(01)00114-6)

- [17] R. Baker, M. Dexter, T. E. Hardwicke, A. Goldstone, and Z. Kourtzi, "Learning to predict: Exposure to temporal sequences facilitates prediction of future events," *Vision Research*, vol. 99, no. 1, pp. 124–133, 2014. Available: <http://dx.doi.org/10.1016/j.visres.2013.10.017>
- [18] P. Perruchet and S. Pacton, "Implicit learning and statistical learning: One phenomenon, two approaches," *Trends in Cognitive Sciences*, vol. 10, no. 5, pp. 233–238, 2006. Available: <http://dx.doi.org/10.1016/j.tics.2006.03.006>
- [19] R. N. Aslin and E. L. Newport, "Statistical learning: From acquiring specific items to forming general rules," *Current Directions in Psychological Science*, vol. 21, no. 3, pp. 170–176, 2012. Available: <http://dx.doi.org/10.1177/0963721412436806>
- [20] T. F. Brady and M. M. Chun, "Spatial constraints on learning in visual search: Modeling and contextual cuing," *Journal of Experimental Psychology: Human Perception and Performance*, vol. 33, no. 4, pp. 798–815, 2007. Available: <http://dx.doi.org/10.1037/0096-1523.33.4.798>
- [21] O. Güler, "New proximal point algorithms for convex minimization," *SIAM Journal on Optimization*, vol. 2, no. 3, pp. 649–664, 1992. Available: <http://dx.doi.org/10.1137/0802032>
- [22] A. Beck and M. Teboulle, "A fast iterative shrinkage-thresholding algorithm for linear inverse problems," *SIAM Journal of Imaging Sciences*, vol. 2, no. 1, pp. 183–202, 2009. Available: <http://dx.doi.org/10.1137/080716542>
- [23] A. Chambolle and C. Dossal, "On the convergence of the iterates of the 'fast iterative shrinkage/thresholding algorithm'," *Journal of Optimization Theory and Applications*, vol. 166, no. 1, pp. 968–982, 2015. Available: <http://dx.doi.org/10.1007/s10957-015-0746-4>
- [24] H. Attouch and J. Peypouquet, "The rate of convergence of Nesterov's accelerated forward-backward method is actually faster than $1/k^2$," *SIAM Journal on Optimization*, vol. 26, no. 3, pp. 1824–1834, 2016. Available: <http://dx.doi.org/10.1137/15M1046095>
- [25] E. Santana, M. S. Emigh, P. Zegers, and J. C. Príncipe, "Exploiting spatio-temporal structure with recurrent winner-take-all networks," *IEEE Transactions on Neural Networks and Learning Systems*, vol. 29, no. 8, pp. 3738–3746, 2018. Available: <http://dx.doi.org/10.1109/TNNLS.2017.2735903>
- [26] J. V. Stone, "Learning perceptually salient visual patterns using spatiotemporal smoothness constraints," *Neural Computation*, vol. 8, no. 7, pp. 1463–1492, 2008. Available: <http://dx.doi.org/10.1162/neco.1996.8.7.1463>
- [27] H. E. Schendan and C. E. Stern, "Where vision meets memory: Prefrontal-posterior networks for visual object constancy during categorization and memory," *Cerebral Cortex*, vol. 18, no. 7, pp. 1695–1711, 2008. Available: <http://dx.doi.org/10.1093/cercor/bhm197>
- [28] J. Sulam, V. Pappayan, Y. Romano, and M. Elad, "Multilayer convolutional sparse modeling: Pursuit and dictionary learning," *IEEE Transactions on Signal Processing*, vol. 66, no. 15, pp. 4090–4104, 2018. Available: <http://dx.doi.org/10.1109/TSP.2018.2846226>
- [29] B. A. Olshausen and D. J. Field, "Emergence of simple-cell receptive field properties by learning a sparse code for natural images," *Nature*, vol. 381, no. 6583, pp. 607–609, 1996. Available: <http://doi.org/10.1038/381607a0>
- [30] Y. Karklin and M. S. Lewicki, "A hierarchical Bayesian model for learning nonlinear statistical regularities in nonstationary natural signals," *Neural Computation*, vol. 17, no. 2, pp. 397–423, 2006. Available: <http://dx.doi.org/10.1162/0899766053011474>
- [31] M. Ito and H. Komatsu, "Representation of angles embedded within contour stimuli in area V2 of macaque monkeys," *Journal of Neuroscience*, vol. 24, no. 13, pp. 3313–3324, 2004. Available: <http://dx.doi.org/10.1523/jneurosci.4364-03.2004>
- [32] J. Hurri and A. Hyvärinen, "Temporal coherence, natural image sequences, and the visual cortex," in *Advances in Neural Information Processing Systems (NIPS)*, S. Becker, S. Thrun, and K. Obermayer, Eds. Cambridge, MA, USA: MIT Press, 2003, pp. 157–164.
- [33] D. P. Kingma and J. Ba, "ADAM: A method for stochastic optimization," in *Proceedings of the International Conference on Learning Representations (ICLR)*, San Diego, CA, USA, May 7–9 2015, pp. 1–15. Available: <https://arxiv.org/abs/1412.6980>
- [34] M. Hardt, B. Recht, and Y. Singer, "Train faster, generalize better: Stability of stochastic gradient descent," in *Proceedings of the International Conference on Machine Learning (ICML)*, New York, NY, USA, June 19–24 2016, pp. 1225–1234.
- [35] O. Sener, H. O. Song, A. Saxena, and S. Savarese, "Learning transferrable representations for unsupervised domain adaptation," in *Advances in Neural Information Processing Systems (NIPS)*, T. G. Dietterich, S. Becker, and Z. Ghahramani, Eds. Red Hook, NY, USA: Curran Associates, 2016, pp. 2110–2118.
- [36] A. Mechelli, C. J. Price, K. J. Friston, and A. Ishai, "Where bottom-up meets top-down: Neuronal interactions during perception and imagery," *Cerebral Cortex*, vol. 14, no. 11, pp. 1256–1265, 2004. Available: <http://dx.doi.org/10.1093/cercor/bhh087>
- [37] M. Bar, "Visual objects in context," *Nature Reviews Neuroscience*, vol. 5, no. 8, pp. 617–629, 2004. Available: <http://dx.doi.org/10.1038/nrn1476>
- [38] J. T. Serences, "Value-based modulations in human visual cortex," *Neuron*, vol. 60, no. 6, pp. 1169–1181, 2008. Available: <http://dx.doi.org/10.1016/j.neuron.2008.10.051>
- [39] S. Ullman, "Sequence seeking and counter streams: A computational model for bidirectional information flow in the visual cortex," *Cerebral Cortex*, vol. 5, no. 1, pp. 1–11, 1995. Available: <http://dx.doi.org/10.1093/cercor/5.1.1>
- [40] M. C. Potter, "Meaning in visual search," *Science*, vol. 187, no. 4180, pp. 965–966, 1975. Available: <http://dx.doi.org/10.1126/science.1145183>
- [41] S. E. Palmer, "The effects of contextual scenes on the identification of objects," *Memory and Cognition*, vol. 3, no. 1, pp. 519–526, 1975. Available: <http://dx.doi.org/10.3758/BF03197524>
- [42] D. H. Hubel and T. N. Wiesel, "Receptive fields and functional architecture in two nonstriate visual areas (18 and 19) of the cat," *Journal of Neurophysiology*, vol. 28, no. 2, pp. 229–289, 1965. Available: <http://dx.doi.org/10.1152/jn.1965.28.2.229>
- [43] —, "Receptive fields and functional architecture of monkey striate cortex," *Journal of Physiology*, vol. 195,

- no. 1, pp. 215–243, 1968. Available: <http://dx.doi.org/10.1113/jphysiol.1968.sp008455>
- [44] S. O. Murray, P. Schrater, and D. Kersten, “Perception grouping and the interactions between visual cortical areas,” *Neural Networks*, vol. 17, no. 5-6, pp. 695–705, 2004. Available: <http://dx.doi.org/10.1016/j.neunet.2004.03.010>
- [45] B. A. Olshausen and D. J. Field, “Sparse coding with an overcomplete basis set: A strategy employed by V1?” *Vision Research*, vol. 37, no. 23, pp. 3311–3325, 1997. Available: [http://doi.org/10.1016/S0042-6989\(97\)00169-7](http://doi.org/10.1016/S0042-6989(97)00169-7)
- [46] M. Riesenhuber and T. Poggio, “Hierarchical models of object recognition in the cortex,” *Nature Neuroscience*, vol. 2, no. 11, pp. 1019–1025, 1999. Available: <http://dx.doi.org/10.1038/14819>
- [47] B. S. Tjan, V. Lestou, and Z. Kourtzi, “Uncertainty and invariance in the human visual cortex,” *Journal of Neurophysiology*, vol. 96, no. 3, pp. 1556–1568, 2005. Available: <http://dx.doi.org/10.1152/jn.01367.2005>
- [48] J. Hedg  and D. C. van Essen, “Selectivity for complex shapes in primate visual area V2,” *Journal of Neuroscience*, vol. 20, no. 5, pp. 1–6, 2000. Available: <http://dx.doi.org/10.1523/jneurosci.20-05-j0001.2000>
- [49] A. Pasupathy and C. E. Connor, “Responses to contour features in macaque area V4,” *Journal of Neurophysiology*, vol. 82, no. 5, pp. 2490–2502, 1999. Available: <http://dx.doi.org/10.1152/jn.1999.82.5.2490>
- [50] —, “Population coding of shape in area V4,” *Nature Neuroscience*, vol. 5, no. 12, pp. 1332–1338, 2002. Available: <http://dx.doi.org/10.1038/972>
- [51] L. Liu, L. She, M. Chen, T. Liu, H. D. Lu, Y. Dan, and M. Poo, “Spatial structure of neuronal receptive field in awake monkey secondary visual cortex (V2),” *Proceedings of the National Academy of Sciences*, vol. 113, no. 7, pp. 1913–1918, 2016, (accepted, in press). Available: <http://dx.doi.org/10.1073/pnas.1525505113>
- [52] C. Bruce, R. Desimone, and C. G. Gross, “Visual properties of neurons in a polysensory area in superior temporal sulcus of the macaque,” *Journal of Neurophysiology*, vol. 46, no. 2, pp. 369–384, 1981. Available: <http://dx.doi.org/10.1152/jn.1981.46.2.369>
- [53] Y. Miyashita and H. S. Chang, “Neuronal correlate of pictorial short-term memory in the primate temporal cortex,” *Nature*, vol. 331, no. 6151, pp. 68–70, 1988. Available: <http://dx.doi.org/10.1038/331068a0>
- [54] V. Yakovlev, S. Fusi, E. Berman, and E. Zohary, “Inter-trial neuronal activity in inferior temporal cortex: A putative vehicle to generate long-term visual associations,” *Nature Neuroscience*, vol. 1, no. 4, pp. 310–317, 1998. Available: <http://dx.doi.org/10.1038/1131>
- [55] E. T. Rolls, “Neurophysiological mechanisms underlying face processing within and beyond the temporal cortical visual areas,” *Philosophical Transactions of the Royal Society of London*, vol. 335, no. 1273, pp. 11–20, 1992. Available: <http://dx.doi.org/10.1098/rstb.1992.0002>
- [56] M. J. Tovee, E. T. Rolls, and P. Azzopardi, “Translation invariance in the responses to faces of single neurons in the temporal visual cortical areas of the alert macaque,” *Journal of Neurophysiology*, vol. 72, no. 3, pp. 1049–1060, 1994. Available: <http://dx.doi.org/10.1152/jn.1994.72.3.1049>
- [57] E. Salinas and L. F. Abbott, “Invariant visual responses from attention gain fields,” *Journal of Neurophysiology*, vol. 77, no. 6, pp. 3267–3272, 1997. Available: <http://dx.doi.org/10.1152/jn.1997.77.6.3267>
- [58] E. T. Rolls, G. C. Baylis, and C. M. Leonard, “Role of low and high spatial frequencies in the face-selective responses of neurons in the cortex in the superior temporal sulcus in the monkey,” *Vision Research*, vol. 25, no. 8, pp. 1021–1035, 1985. Available: [http://dx.doi.org/10.1016/0042-6989\(85\)90091-4](http://dx.doi.org/10.1016/0042-6989(85)90091-4)
- [59] L. Liu, J. A. Bourne, and M. G. P. Rosa, “Spatial and temporal frequency selectivity of neurons in the middle temporal visual area of new world monkeys (*Callithrix jacchus*),” *European Journal of Neuroscience*, vol. 25, no. 6, pp. 1780–1792, 2007. Available: <http://dx.doi.org/10.1111/j.1460-9568.2007.05453.x>
- [60] H. Liang, X. Gong, M. Chen, Y. Yan, W. Li, and C. D. Gilbert, “Interactions between feedback and lateral connections in the primary visual cortex,” *Proceedings of the National Academy of Sciences*, vol. 114, no. 32, pp. 8637–8642, 2017. Available: <http://dx.doi.org/10.1073/pnas.1706183114>
- [61] N. Ramalingam, J. N. J. McManus, W. Li, and C. D. Gilbert, “Top-down modulation of lateral interactions in visual cortex,” *Journal of Neuroscience*, vol. 33, no. 5, pp. 1773–1789, 2013. Available: <http://dx.doi.org/10.1523/jneurosci.3825-12.2013>
- [62] B. Epshtein, I. Lifshitz, and S. Ullman, “Image interpretation by a single bottom-up top-down cycle,” *Proceedings of the National Academy of Sciences*, vol. 105, no. 38, pp. 14 298–14 303, 2008. Available: <http://dx.doi.org/10.1073/pnas.0800968105>

Appendix A

Below, we outline the ADPCN training and inference process.

Algorithm 1: Accelerated Deep Prediction Network (ADPCN) Training and Inference

- 1 **Inputs:** Initial dictionary matrix $D_i^\top \in \mathbb{R}_+^{k_i \times k_{i-1}}$, state-transition matrix $C_i \in \mathbb{R}^{k_i \times k_i}$, and invariant matrix $G_i \in \mathbb{R}^{d_i \times k_i}$ for each network layer. A set of time-varying, static stimuli Y_t , where $y_t \in Y_t$, $y_t \in \mathbb{R}^p$. A set of initial states $\gamma_{i,0} \in \mathbb{R}_+^{k_i}$ and causes $\kappa_{i,0} \in \mathbb{R}^{d_i}$.
 - 2 **for** $t = 0, 1, 2, \dots$ **do**
 - 3 Initialize the bottom-up cause for the first layer as $\kappa_{0,t} = y_t$.
 - 4 **for** $i = 0, 1, 2, \dots$ **do**
 - 5 For all layers but the last, the most likely top-down causes, $\kappa'_{i-1,t} \in \mathbb{R}^{d_{i-1}}$, are initialized at each iteration using the previous states $\gamma_{i,t} \in \mathbb{R}^{k_i}$ and the causes $\kappa_{i,t} \in \mathbb{R}^{d_i}$,

$$\kappa'_{i-1,t} = D_i^\top \gamma'_{i,t}, \quad \gamma'_{i,t} = \arg \min_{\gamma_{i,t}} \left(\lambda'_{i,t} \|\gamma_{i,t+1} - C_i \gamma_{i,t}\|_1 + \alpha'_i \|\gamma_{i,t}\|_1 \left(1 + \exp(-\text{UNPOOL}(G_i \kappa_{i,t})) \right) \right).$$

This minimization problem has an algebraic expression for the global solution: $[\gamma'_{i,t}]_k = [C_{i,t} \gamma_{i,t-1}]_k$, whenever $\alpha'_i \lambda_{i,t,k} < \alpha_i$, and zero otherwise. For the last layer, $\kappa'_{i,t+1} = \kappa_{i,t}$.
 - 6 **for** $i = 0, 1, 2, \dots$ **do**
 - 7 Let $\beta_m \in \mathbb{R}_+$ be an inertial sequence, $\beta_m = (k_m - 1)/k_{m+1}$, where $k_m = 1 + (m^r - 1)/d$ with $r \in \mathbb{R}_{1,+}$ and $d \in \mathbb{R}_+$. Given an adjustable step size $\tau_{i,t}^m \in \mathbb{R}_+$, update the states using proximal-gradient steps, indexed by m , until either convergence or a pre-set number of iterations has been reached

$$\gamma_{i,t+1}^m = \text{PROX}_{\lambda_{i,t}} \left(\pi_{i,t}^m - \lambda_{i,t} \tau_{i,t}^m (D_i^\top (\kappa_{i-1,t} - D_i \pi_{i,t}^m) + \alpha_i \Omega_i(\pi_{i,t}^m)) \right),$$

where $\pi_{i,t}^{m+1} = \gamma_{i,t+1}^m + \beta_m (\gamma_{i,t+1}^m - \gamma_{i,t+1}^{m-1})$. The term $\Omega_i(\pi_{i,t}^m)$ quantifies the contribution of the non-smooth state transition. Use Nesterov smoothing, with $\mu_i \in \mathbb{R}_+$, to approximate them, $\Omega_i(\pi_{i,t}) = \arg \max_{\|\Omega_{i,t}\|_\infty \leq 1} \Omega_{i,t}^\top (\pi_{i,t}^m - C_i \gamma_{i,t-1}) - \mu_i \|\Omega_{i,t}\|_2^2/2$. Max-pool the states using non-overlapping windows $\gamma_{i,t+1} = \text{POOL}(\gamma_{i,t+1})$.
 - 8 Let $\beta'_m \in \mathbb{R}_+$ be an inertial sequence, $\beta'_m = (k_m - 1)/k_{m+1}$, where $k_m = 1 + (m^r - 1)/d$ with $r \in \mathbb{R}_{1,+}$, $d \in \mathbb{R}_+$. Given an adjustable step size $\tau'_{i,t} \in \mathbb{R}_+$, update the causes using proximal-gradient steps until either convergence or a pre-set number of iterations has been reached

$$\kappa_{i,t+1}^m = \text{PROX}_{\lambda'_i} \left(\pi_{i,t}^m - \lambda'_i \tau'_{i,t} (2\eta'_i (\kappa_{i,t+1}^m - \kappa'_{i,t}) - \alpha'_i G_i^\top \exp(-G_i \pi_{i,t}^m) |\gamma'_{i,t+1}|) \right),$$

where $\pi_{i,t}^{m+1} = \kappa_{i,t+1}^m + \beta'_m (\kappa_{i,t+1}^m - \kappa_{i,t}^{m-1})$. Update the sparsity parameter using spatial max unpooling after the causes update has concluded, $\lambda_{i,t+1} = \alpha'_i (1 + \exp(-\text{UNPOOL}(G_i \kappa_{i,t+1})))$.
 - 9 **for** $i = 0, 1, 2, \dots$ **do**
 - 10 Update the filter dictionary matrix $D_i^\top \in \mathbb{R}_+^{k_i \times k_{i-1}}$ and the state-transition matrix $C_{i,t} \in \mathbb{R}^{k_i \times k_i}$ independently, until either convergence or a pre-set number of iterations has been reached, via dual-estimation filtering, with steps indexed by m ,

$$D_i^{m+1\top} = D_i^m + \sigma_t + \psi_i^m \left((\gamma_{i-1,t+1} - D_i^m \gamma_{i,t+1}) \gamma_{i,t+1} + \theta_i^m (D_i^m - D_i^{m-1}) \right),$$

$$C_i^{m+1} = C_i^m + \sigma'_t + \psi_i^m \left(\text{SIGN}(\gamma_{i,t+1} - C_i^m \gamma_{i,t}) \gamma_{i,t+1}^\top + \theta_i^m (C_i^m - C_i^{m-1}) \right),$$

where $\psi_i^m, \psi_i'^m \in \mathbb{R}_+$ are step sizes, $\theta_i^m \in \mathbb{R}_+$ is a momentum coefficient, and $\sigma_t, \sigma'_t \in \mathbb{R}$ is Gaussian transition noise over the parameters. Normalize $D_i^{m+1\top}$ to avoid returning a trivial solution.
 - 11 Update the causal invariance matrix $G_i \in \mathbb{R}^{d_i \times k_i}$ via dual-estimation filtering, with steps indexed by m ,

$$G_i^{m+1} = G_i^m + \sigma''_t + \psi_i^m \left((\exp(-G_i^m \kappa_{i+1,t}) |\gamma_{i,t+1}|) \kappa_{i,t+1}^\top + \theta_i^m (G_i^m - G_i^{m-1}) \right),$$

where $\psi_i^m \in \mathbb{R}_+$ is a step size, $\theta_i^m \in \mathbb{R}_+$ is a momentum coefficient, and $\sigma''_t \in \mathbb{R}$ is Gaussian-distributed transition noise over the parameters. Normalize G_i^{m+1} to avoid returning a trivial solution.
-

The convergence of dual-estimation filtering is straightforward to demonstrate. For the proximal-gradient inference process, it is much more involved. We build up to it in what follows. We first prove a weak convergence result that facilitates demonstrating a much stronger one when relying on properties of Cauchy sequences. We then quantify the global convergence rate for our chosen inertial sequence. We then compare the global convergence rate to

a Nesterov-style inertial sequence that was used in the original DPCN to illustrate the advantages of the former for ADPCNs. Lastly, we outline local convergence properties of both inertial sequences to explain the results presented for DPCNs and ADPCNs in the main part of the paper.

Toward this end, it is important to show that the distance between a given iterate and the solution set for either inference cost can be bounded by the norm of the residual. This occurs whenever the norm of the residual is small. The iterate must also be sufficiently close to the solution set.

Proposition A.1. Let $\gamma_{i,t} \in \mathbb{R}_+^{k_i}$ be the hidden states and $\kappa_{i,t} \in \mathbb{R}^{d_i}$ be the hidden causes. Let $\pi_{i,t} \in \mathbb{R}_+^{k_i}$ be the auxiliary states and let $\pi'_{i,t} \in \mathbb{R}^{d_i}$ be the auxiliary causes at layer i and time t . Let $\omega_{1,i} \in \mathbb{R}$, that is assumed to satisfy $\omega_{1,i} \geq \mathcal{L}_1(\gamma_{i,t}^*, \kappa_{i,t}, C_i, D_i^\top; \alpha_i, \lambda_i)$. As well, let $\omega_{2,i} \in \mathbb{R}$, $\omega_{2,i} \geq \mathcal{L}_2(\gamma_{i,t}, \kappa_{i,t}^*, G_i; \alpha'_i, \lambda'_i, \eta'_i, \lambda_{i,t})$. For some $\omega_{1,i}$, there are $\epsilon_{1,i}, \epsilon'_{1,i} \in \mathbb{R}_+$, such that, for step size $\tau_{i,t}^m \in \mathbb{R}_+$

$$\text{dist}(\gamma_{i,t+1}^m, \Gamma_i^*) \leq \epsilon'_{1,i} \left\| \text{PROX}_{\lambda_{i,t}/\ell_{i,j}} \left(\pi_{i,t}^m - \lambda_{i,t} \tau_{i,t}^m \nabla \pi_{i,t}^m \mathcal{L}_1(\pi_{i,t}^m, \kappa_{i,t}, C_i, D_i^\top; \alpha_i, \lambda_i) \right) - \pi_{i,t}^m \right\|$$

whenever the following conditions, $\| \text{PROX}_{\lambda_{i,t}}(\pi_{i,t}^m - \lambda_{i,t} \tau_{i,t}^m \nabla \pi_{i,t}^m \mathcal{L}_1(\pi_{i,t}^m, \kappa_{i,t}, C_i, D_i^\top; \alpha_i, \lambda_{i,t})) - \gamma_{i,t}^m \| < \epsilon_{1,i}$ and $\omega_{1,i} \leq \mathcal{L}_1(\gamma_{i,t}^m, \kappa_{i,t}, C_i, D_i^\top; \alpha_i, \lambda_i)$, are satisfied. Here, $\text{dist}(\gamma_{i,t+1}^m, \Gamma_i^*)$ denotes the distance of a given iterate with the solution set. Likewise, for some $\omega_{2,i}$, there are $\epsilon_{2,i}, \epsilon'_{2,i} \in \mathbb{R}_+$, such that, for step sizes $\tau_{i,t}^m \in \mathbb{R}_+$,

$$\text{dist}(\kappa_{i,t}^m, K_i^*) \leq \epsilon'_{2,i} \left\| \text{PROX}_{\lambda'_{i,j}/\ell'_{i,j}} \left(\pi'_{i,t}^m - \lambda'_{i,t} \tau_{i,t}^m \nabla \pi'_{i,t}^m \mathcal{L}_2(\gamma_{i,t+1}, \pi'_{i,t}^m, G_i; \alpha'_i, \lambda'_i, \eta'_i, \lambda_{i,t}) \right) - \pi'_{i,t}^m \right\|$$

whenever the following conditions $\| \text{PROX}_{\lambda_{i,t}}(\pi'_{i,t}^m - \lambda'_{i,t} \tau_{i,t}^m \nabla \pi'_{i,t}^m \mathcal{L}_2(\gamma_{i,t+1}, \pi'_{i,t}^m, G_i; \alpha'_i, \lambda'_i, \eta'_i, \lambda_{i,t})) - \kappa_{i,t}^m \| < \epsilon_{2,i}$ and $\omega_{2,i} \leq \mathcal{L}_2(\gamma_{i,t+1}, \pi'_{i,t}^m, G_i; \alpha'_i, \lambda'_i, \eta'_i, \lambda_{i,t})$ are satisfied. Here, Γ_i^* , with $\gamma_i^* \in \Gamma_i^*$, $\gamma_i^* \in \mathbb{R}_+^{k_i}$, denotes the solution set for the state-inference cost function. As well, K_i^* , with $\kappa_i^* \in K_i^*$, $\kappa_i^* \in \mathbb{R}_+^{d_i}$, denotes the solution set for the cause-inference cost function. Both $\ell_{i,j}, \ell'_{i,j} \in \mathbb{R}_+$ denote Lipschitz constants of the state and cause costs.

Proof: In what follows, for ease of presentation, we ignore the variables of the inference cost that remain fixed across inference iterations. Let the L_1 -sparsity term in the state-inference cost be re-written in an equivalent manner as $\sum_{k'=1}^{k_i} [\lambda_{i,t}]_{k'} \xi_{i,t}$, with the polyhedral-set constraint $|\gamma_{i,t}]_{k'}| - \xi_{i,t} \leq 0$, $\xi_{i,t} \in \mathbb{R}^{k_i}$. There exists some $\omega_i \in [0, \infty)^{k_i}$ such that

$$(\text{PROX}_{\lambda_{i,t}/\ell_{i,j}}(\pi_{i,t}^m - \lambda_{i,t} \tau_{i,t}^m \nabla \pi_{i,t}^m \mathcal{L}_1(\pi_{i,t}^m)) - \gamma_{i,t}^m) + (\nabla \pi_{i,t}^m \mathcal{L}_1(\pi_{i,t}^m) - \omega_i) = 0,$$

where $(\text{PROX}_{\lambda_{i,t}/\ell_{i,j}}(\pi_{i,t}^m - \lambda_{i,t} \tau_{i,t}^m \nabla \pi_{i,t}^m \mathcal{L}_1(\pi_{i,t}^m)) - \gamma_{i,t}^m) = \xi_{i,t}$. Here, we assume that the choice of $\pi_{i,t}^m$ is such that the inequality conditions are satisfied for $\epsilon_{1,i}, \epsilon'_{1,i} \in \mathbb{R}_+$. As well, there exists some optimal $\pi_i^* \in \Gamma_i^*$, $\pi_i^* \in \mathbb{R}_+^{k_i}$, and a corresponding $\omega_i^* \in [0, \infty)^{k_i}$ such that $\nabla \pi_i^* \mathcal{L}_1(\pi_i^*) - \omega_i^* = 0$, where $\pi_i^* = \xi_{i,t}$. We also have that, for $\sigma \in \mathbb{R}_+$, $2\sigma \|\pi_{i,t}^m - \pi_i^*\|^2 \leq \langle \pi_{i,t}^m - \pi_i^*, \nabla \pi_{i,t}^m \mathcal{L}_1(\pi_{i,t}^m) - \nabla \pi_i^* \mathcal{L}_1(\pi_i^*) \rangle$. Hence, for some $\omega'_{1,i} \in \mathbb{R}$ that depends on $\omega_{1,i} \in \mathbb{R}$, we have

$$2\sigma \|\pi_{i,t}^m - \pi_i^*\| \leq (\omega'_{1,i} + ((\omega'_{1,i})^2 + 4\omega'_{1,i})^{1/2}) \|\pi_{i,t}^m - \text{PROX}_{\lambda_{i,t}/\ell_{i,j}}(\pi_{i,t}^m - \lambda_{i,t} \tau_{i,t}^m \nabla \pi_{i,t}^m \mathcal{L}_1(\pi_{i,t}^m))\|/2.$$

When combined with $\|(\pi_{i,t}^m, \omega_{i,t}) - (\pi_i^*, \omega_i^*)\| \leq \delta_i (\|\pi_{i,t}^m - \pi_i^*\| + \|\pi_{i,t}^m - \text{PROX}_{\lambda_{i,t}}(\pi_{i,t}^m - \lambda_{i,t} \tau_{i,t}^m \nabla \pi_{i,t}^m \mathcal{L}_1(\pi_{i,t}^m))\|)$ for $\delta_i \in \mathbb{R}_+$, we get that $\min_{\pi^* \in \Gamma_i^*} \|\pi_{i,t}^m - \pi^*\| \leq \epsilon'_{1,i} \|\pi_{i,t}^m - \pi_i^*\|$. A similar argument to what is above can be used for the causes. ■

As Luo and Tseng [1] have shown, such locally held bounds are useful for analyzing the rate of convergence of iterative algorithms. They can be used to very weakly demonstrate that the sequence of functional iterates will eventually reach the global functional solution, albeit independent of strong inertial-sequence properties. Analogous bounds have been derived by Pang [2], albeit for strongly convex problems. Here, we do not impose the condition of strong convexity for the inference costs, which makes these results applicable to a broader set of functionals, much like the ones that we employ.

To provide a more general convergence result, we need to consider specific inertial sequences and incorporate them into the analysis. Toward this end, we first bound the squared residual between the primary iterates, the states $\gamma_{i,t}$ and the causes $\kappa_{i,t}$, and their corresponding auxiliary iterates $\pi_{i,t}$ and $\pi'_{i,t}$.

Proposition A.2. Let $\gamma_{i,t} \in \mathbb{R}_+^{k_i}$ be the hidden states and $\kappa_{i,t} \in \mathbb{R}^{d_i}$ be the hidden causes. Let $\pi_{i,t} \in \mathbb{R}_+^{k_i}$ be the auxiliary states at layer i and time t . Assume that the state update, for a positive step size $\tau_{i,t}^m \in \mathbb{R}_+$, is given by the relation $\gamma_{i,t+1}^m = \text{PROX}_{\lambda_{i,t}}(\pi_{i,t}^m - \lambda_{i,t} \tau_{i,t}^m \nabla \pi_{i,t}^m \mathcal{L}_1(\pi_{i,t}^m, \kappa_{i,t}, C_i, D_i^\top; \alpha_i, \lambda_{i,t}))$, with the auxiliary state update $\pi_{i,t}^{m+1} = \gamma_{i,t+1}^m + \beta_m(\gamma_{i,t+1}^m - \gamma_{i,t+1}^{m-1})$. Likewise, assume that the cause update, for a positive step size $\tau_{i,t}^m \in \mathbb{R}_+$, is given by the relation $\pi'_{i,t+1}^m = \text{PROX}_{\lambda'_{i,t}}(\pi'_{i,t}^m - \lambda'_{i,t} \tau_{i,t}^m \nabla \pi'_{i,t}^m \mathcal{L}_2(\gamma_{i,t+1}, \pi'_{i,t}^m, G_i; \alpha'_i, \lambda'_i, \eta'_i, \lambda_{i,t}))$, with the auxiliary cause relation $\pi'_{i,t}^{m+1} = \kappa_{i,t+1}^m + \beta'_m(\kappa_{i,t+1}^m - \kappa_{i,t+1}^{m-1})$. In both cases, let $\beta_m, \beta'_m = (k_m - 1)/k_{m+1}$, with elements

$k_m = 1 + (m^r - 1)/d$ with $r \in \mathbb{R}_{1,+}$, $d \in \mathbb{R}_+$. There are some $\epsilon_{1,i}, \epsilon_{2,i} \in \mathbb{R}_+$ such that

$$\begin{aligned} \|\pi_{i,t}^m - \gamma_{i,t+1}^m\|^2 &\geq \frac{\tau_{i,t}^m}{\epsilon_{1,i}} \left(\mathcal{L}_1(\gamma_{i,t+1}^m, \kappa_{i,t}, C_i, D_i^\top; \alpha_i, \lambda_{i,t}) - \mathcal{L}_1(\gamma_i^*, \kappa_{i,t}, C_i, D_i^\top; \alpha_i, \lambda_{i,t}) \right) \\ \|\pi_{i,t}'^m - \kappa_{i,t+1}^m\|^2 &\geq \frac{\tau_{i,t}'^m}{\epsilon_{2,i}} \left(\mathcal{L}_2(\gamma_{i,t+1}, \kappa_{i,t+1}^m, G_i; \alpha_i', \lambda_i', \eta_i', \lambda_{i,t}) - \mathcal{L}_2(\gamma_{i,t+1}, \kappa_i^*, G_i; \alpha_i', \lambda_i', \eta_i', \lambda_{i,t}) \right) \end{aligned}$$

where $\gamma_i^* \in \Gamma_i^*$, $\gamma_i^* \in \mathbb{R}_+^{k_i}$, is a solution of the state-inference cost and $\kappa_i^* \in K_i^*$, $\kappa_i^* \in \mathbb{R}_+^{d_i}$, is a solution of the cause-inference cost.

Proof: We focus on the case of the hidden states; that for the hidden causes has only slight differences. In what follows, for ease of presentation, we ignore the variables of the inference cost that remain fixed across inference iterations. We have, for m being sufficiently large, that

$$\begin{aligned} \mathcal{L}_1(\gamma_{i,t+1}^m) - \mathcal{L}_1(\gamma_i^*) &\leq 2\|\gamma_{i,t+1}^{m+1} - \pi_{i,t}^{m+1}\|^2 / \tau_{i,t}^m + \text{dist}(\gamma_{i,t+1}^{m+1}, \Gamma_i^*) \|\gamma_{i,t+1}^{m+1} - \pi_{i,t}^{m+1}\| / \tau_{i,t}^m \\ &\leq \xi_{1,i}^{-1} (4\epsilon_{1,i}'' + \xi_{1,i}) \|\gamma_{i,t+1}^{m+1} - \pi_{i,t}^{m+1}\|^2 / 2\tau_{i,t}^m \end{aligned}$$

where $\epsilon_{1,i}'' \in \mathbb{R}_+$ and $\xi_{1,i} \in \mathbb{R}_+$. There exists some $\epsilon_{1,i} \geq \xi_{1,i}^{-1} (4\epsilon_{1,i}'' + \xi_{1,i})/2$, which must naturally be positive, such that the proposition is true. Here, the second inequality follows from proposition A.1,

$$\text{dist}(\gamma_{i,t+1}^m, \Gamma_i^*) \leq \epsilon_{1,i}' \|\text{PROX}_{\tau_{i,t}^m}(\gamma_{i,t+1}^m - \lambda_{i,t} \tau_{i,t}^m \nabla \gamma_{i,t+1}^m \mathcal{L}_1(\gamma_{i,t+1}^m) - \gamma_{i,t+1}^m) / \ell_{i,t} \tau_{i,t}^m\|,$$

This arises from the non-decreasing nature of the proximal-norm function and the Cauchy-Schwarz inequality, which implies that dividing by $\ell_{i,t} \tau_{i,t}^m$ leads to a non-increasing function. The iterate-solution distance can thus be further bounded from above as $\text{dist}(\gamma_{i,t+1}^m, \Gamma_i^*) \leq 2\epsilon_{1,i}' \xi_{1,i} \|\gamma_{i,t+1}^m - \pi_{i,t}^m\|$. Since the relationship holds for arbitrary m sufficiently large, it can be increased by one iteration. ■

We now can bound the functional-value difference between an arbitrary iterates, $\gamma_{i,t}$ and $\kappa_{i,t}$, and optimal solutions, $\gamma_i^* \in \Gamma_i^*$ and $\kappa_i^* \in K_i^*$. Note that, due to convexity of the two inference costs, every solution is guaranteed to be a globally optimal one. From this result, we will be able to obtain convergence of the function values and iterates.

Proposition A.3. Let $\gamma_{i,t} \in \mathbb{R}_+^{k_i}$ be the hidden states and $\kappa_{i,t} \in \mathbb{R}_+^{d_i}$ be the hidden causes. Let the inertial sequences used, respectively, for the state-inference and cause-inference costs be $\beta_m, \beta_m' = (k_m - 1)/k_{m+1}$, where $k_m = 1 + (m^r - 1)/d$ with $r \in \mathbb{R}_{1,+}$, $d \in \mathbb{R}_+$. We have that

$$\begin{aligned} &\sum_{m=1}^{\infty} k_{m+1}^2 \left(\mathcal{L}_1(\gamma_{i,t+1}^m, \kappa_{i,t}, C_i, D_i^\top; \alpha_i, \lambda_{i,t}) - \mathcal{L}_1(\gamma_i^*, \kappa_{i,t}, C_i, D_i^\top; \alpha_i, \lambda_{i,t}) \right) \\ &\sum_{m=1}^{\infty} k_{m+1}^2 \left(\mathcal{L}_2(\gamma_{i,t+1}, \kappa_{i,t+1}^m, G_i; \alpha_i', \lambda_i', \eta_i', \lambda_{i,t}) - \mathcal{L}_2(\gamma_{i,t+1}, \kappa_i^*, G_i; \alpha_i', \lambda_i', \eta_i', \lambda_{i,t}) \right) \end{aligned}$$

are convergent. Here, $\gamma_i^* \in \Gamma_i^*$, $\gamma_i^* \in \mathbb{R}_+^{k_i}$, is a solution of the state-inference cost and $\kappa_i^* \in K_i^*$, $\kappa_i^* \in \mathbb{R}_+^{d_i}$, is a solution of the cause-inference cost. We have assumed, here, that the state update, for a positive step size $\tau_{i,t}^m \in \mathbb{R}_+$, was given by the relation $\gamma_{i,t+1}^m = \text{PROX}_{\lambda_{i,t}}(\pi_{i,t}^m - \lambda_{i,t} \tau_{i,t}^m \nabla \pi_{i,t}^m \mathcal{L}_1(\pi_{i,t}^m, \kappa_{i,t}, C_i, D_i^\top; \alpha_i, \lambda_{i,t}))$, with the auxiliary update $\pi_{i,t}^{m+1} = \gamma_{i,t+1}^m + \beta_m(\gamma_{i,t+1}^m - \gamma_{i,t+1}^{m-1})$. As well, the cause update, for a positive step size $\tau_{i,t}'^m \in \mathbb{R}_+$, was $\kappa_{i,t+1}^m = \text{PROX}_{\lambda_i'}(\pi_{i,t}'^m - \lambda_i' \tau_{i,t}'^m \nabla \pi_{i,t}'^m \mathcal{L}_2(\gamma_{i,t+1}, \pi_{i,t}'^m, G_i; \alpha_i', \lambda_i', \eta_i', \lambda_{i,t}))$, with the auxiliary cause update $\pi_{i,t}'^{m+1} = \kappa_{i,t+1}^m + \beta_m'(\kappa_{i,t+1}^m - \kappa_{i,t+1}^{m-1})$.

Proof: For ease of presentation, we ignore the variables of the inference cost that remain fixed across inference iterations. It can be shown that, for some $\xi_{1,i} \in \mathbb{R}_+$,

$$\begin{aligned} \mathcal{L}_1(\gamma_{i,t+1}^{m+1}) &\leq \mathcal{L}_1(\gamma_{i,t+1}^m) - \|\gamma_{i,t+1}^{m+1} - \gamma_{i,t+1}^m\|^2 / 2\tau_{i,t}^m + \|\gamma_{i,t+1}^m - \pi_{i,t}^{m+1}\|^2 / 2\tau_{i,t}^m - (1 - \xi_{1,i}) \|\gamma_{i,t+1}^{m+1} - \pi_{i,t}^{m+1}\|^2 / \tau_{i,t}^m \\ &\leq (1 - \beta_{m+1}^{-1}) \mathcal{L}_1(\gamma_{i,t}^m) + \beta_{m+1} \mathcal{L}_1(\gamma_i^*) + \beta_{m+1}^{-2} \|\beta_m \gamma_{i,t+1}^{m+1} - (\beta_{m+1} - 1) \gamma_{i,t+1}^m - \gamma_i^*\|^2 / 2\tau_{i,t}^m \\ &\quad + \beta_{m+1}^{-2} \|\beta_m \gamma_{i,t+1}^m - (\beta_m - 1) \gamma_{i,t+1}^{m-1} - \gamma_i^*\|^2 / 2\tau_{i,t}^m - (1 - \xi_{1,i}) \|\gamma_{i,t+1}^{m+1} - \pi_{i,t}^{m+1}\|^2 / \tau_{i,t}^m \end{aligned}$$

where $\gamma_{i,t+1}'^m = \beta_{m+1}^{-1} \gamma_i^* + (1 - \beta_{m+1}^{-1}) \gamma_{i,t}^m$. Multiplying both sides by k_{m+1}^2 and re-arranging terms yields

$$\begin{aligned} &k_{m+1}^2 (\mathcal{L}_1(\gamma_{i,t+1}^k) - \mathcal{L}_1(\gamma_i^*)) - k_{m+1}^2 (\mathcal{L}_1(\gamma_{i,t+1}^m) - \mathcal{L}_1(\gamma_i^*)) \\ &\geq (k_m^2 - k_{m+1}^2 - k_{m+1}) (\mathcal{L}_1(\gamma_{i,t+1}^m) - \mathcal{L}_1(\gamma_i^*)) + k_{m+1}^2 (1 - \xi_{1,i}) \|\gamma_{i,t+1}^m - \pi_{i,t}^m\|^2 / 2\tau_{i,t}^m \\ &\quad - \|k_{m+1} \gamma_{i,t+1}^{m+1} - (k_{m+1} - 1) \gamma_{i,t+1}^m - \gamma_i^*\|^2 / \tau_{i,t}^m - \|k_m \gamma_{i,t+1}^m - (k_m - 1) \gamma_{i,t+1}^{m-1} - \gamma_i^*\|^2 / \tau_{i,t}^m. \end{aligned}$$

The result derived in proposition A.2 can be applied to show that $k_{m+1}^2 (1 - \xi_{1,i}) \|\gamma_{i,t+1}^m - \pi_{i,t}^m\|^2 / 2\tau_{i,t}^m$ is bounded

above by $k_{m+1}^2(1-\xi_{i,t})(\mathcal{L}_1(\gamma_{i,t+1}^{m+1})-\mathcal{L}_1(\gamma_i^*))/4\epsilon_{1,i}$. Continuing from above, we have that

$$\begin{aligned} & (2k_m^2 - k_{m+1}^2 - k_{m+1})(\mathcal{L}_1(\gamma_{i,t+1}^m) - \mathcal{L}_1(\gamma_i^*)) - (k_m^2 - k_{m+1})(\gamma_{i,t+1}^{m+1} - \mathcal{L}_1(\gamma_i^*)) \\ & \geq (k_m^2 - k_{m+1}^2 - k_{m+1})(\mathcal{L}_1(\gamma_{i,t+1}^m) - \mathcal{L}_1(\gamma_i^*)) + k_{m+1}^2(1-\xi_{i,t})\|\gamma_{i,t+1}^m - \pi_{i,t}^m\|^2/2\tau_{i,t}^m \\ & \quad + k_{m+1}^2(1-\xi_{i,t})\|\gamma_{i,t+1}^{m+1} - \pi_{i,t}^{m+1}\|^2/4\tau_{i,t}^m. \end{aligned}$$

From this, we can see that $(2k_m^2 - k_{m+1}^2 - k_{m+1})(\mathcal{L}_1(\gamma_{i,t+1}^m) - \mathcal{L}_1(\gamma_i^*)) + k_{m+1}^2(1-\xi_{i,t})\|\gamma_{i,t+1}^m - \pi_{i,t}^m\|^2/2\tau_{i,t}^m$ is a non-increasing sequence for m . It is bounded below. This implies convergence of the sequence in m and hence for $m+1$. This takes care of the two terms on the left and the first two terms on the right-hand side. This leaves the final term on the right-hand side, $k_{m+1}^2(1-\xi_{i,t})\|\gamma_{i,t+1}^{m+1} - \pi_{i,t}^{m+1}\|^2/4\tau_{i,t}^m$, which is also convergent in m .

Applying proposition A.2 to this final term on the right-hand side proves the proposition for the hidden states. A similar argument to what is above can be used for the causes. ■

Based on properties of the inertial series $\{\beta_m\}_{m=1}^\infty$ and $\{\beta'_m\}_{m=1}^\infty$, particularly that the inverse of the inertial subcomponents $\sum_{m=1}^\infty k_m^{-1}$ is convergent, we immediately obtain that the state $\{\gamma_{i,t}^m\}_{m=1}^\infty$ and cause $\{\kappa_{i,t}^m\}_{m=1}^\infty$ iterates are Cauchy. The state and cause iterates are thus bounded. The Bolzano-Weierstrass theorem implies convergence of iterate subsequences for complete spaces, which applies to our case. The iterates themselves are also strongly convergent to global solutions. Convergence of proximal-gradient-type schemes is not new. It, however, needed to be verified for our accelerated case.

We are now able to prove the main convergence result of the paper.

Proposition 4. Let $\gamma_{i,t} \in \mathbb{R}_+^{k_i}$ be the hidden states and $\kappa_{i,t} \in \mathbb{R}^{d_i}$ be the hidden causes. The state iterates $\{\gamma_{i,t+1}^m\}_{m=1}^\infty$ strongly converge to the global solution of $\mathcal{L}_1(\gamma_{i,t}, \kappa_{i,t}, C_i, D_i^\top; \alpha_i, \lambda_{i,t})$ for the accelerated proximal gradient scheme. Likewise, the cause iterates $\{\kappa_{i,t+1}^m\}_{m=1}^\infty$ for the accelerated proximal gradient scheme strongly converge to the global solution of $\mathcal{L}_2(\gamma_{i,t+1}, \kappa_{i,t}, G_i; \alpha'_i, \lambda'_i, \eta'_i, \lambda_{i,t})$ at a sub-polynomial rate. This occurs when using the inertial sequences $\beta_m, \beta'_m = (k_m - 1)/k_{m+1}$, where k_m depends polynomially on m .

Proof: Strong convergence of the states $\{\gamma_{i,t+1}^m\}_{m=1}^\infty$ and causes $\{\kappa_{i,t+1}^m\}_{m=1}^\infty$ to the optimal solutions $\gamma_i^* \in \Gamma_i^*$ and $\kappa_i^* \in K_i^*$ can be obtained from an extension of proposition A.3. For the convergence rate, we note that there is some $\zeta_i \in \mathbb{R}_+$ such that $\zeta_i m^{-r} \geq \|\gamma_{i,t+1}^{m-1} - \gamma_{i,t}^m\|$. For $m' > 1$, we have that $\|\gamma_{i,t+1}^{m+m'} - \gamma_{i,t}^m\|$ is bounded above by $\sum_{j=m+1}^{m+m'} \|\gamma_{i,t}^j - \gamma_{i,t}^{j-1}\| \leq \zeta_i \sum_{j=m+1}^{m+m'} m^{-r}$. As $m' \rightarrow \infty$, $\|\gamma_{i,t+1}^m - \gamma_i^*\| \leq \zeta_i r/m^r(r-1)$, which implies a sub- r -polynomial rate of convergence for the state iterate sequence. A similar result holds for the cause iterates. ■

The choice of the inertial sequence greatly affects convergence properties. The classical sequence proposed by Nesterov, for instance, yields iterates $\{\gamma_{i,t+1}^m\}_{m=1}^\infty$ and $\{\kappa_{i,t+1}^m\}_{m=1}^\infty$ that only weakly converge to global solutions $\gamma_i^* \in \Gamma_i^*$ and $\kappa_i^* \in K_i^*$, which stems from the fact that $\sum_{m=1}^\infty k_m^{-1}$, with $k_{m+1} = (1 + (1 + 4k_m^2)^{1/2})/2$, is divergent. In finite-dimensional Euclidean spaces, this is not a shortcoming, since it implies convergence componentwise and thus is equivalent to strong convergence.

The original DPCN relied on a Nesterov-style sequence, so we analyze its convergence.

Proposition A.4. Let the inertial sequences used, respectively, for the state-inference and cause-inference costs be $\beta_m, \beta'_m = (k_m - 1)/k_{m+1}$, where $k_{m+1} = (1 + (1 + 4k_m^2)^{1/2})/2$. We have that

$$\begin{aligned} & \sum_{m=1}^\infty k_m^2 \left(\mathcal{L}_1(\gamma_{i,t+1}^m, \kappa_{i,t}, C_i, D_i^\top; \alpha_i, \lambda_{i,t}) - \mathcal{L}_1(\gamma_i^*, \kappa_{i,t}, C_i, D_i^\top; \alpha_i, \lambda_{i,t}) + \frac{1}{2\tau_{i,t}^m} \|\gamma_{i,t+1}^m - \gamma_{i,t+1}^{m-1}\|^2 \right) \\ & \sum_{m=1}^\infty k_m^2 \left(\mathcal{L}_2(\gamma_{i,t+1}, \kappa_{i,t+1}^m, G_i; \alpha'_i, \lambda'_i, \eta'_i, \lambda_{i,t}) - \mathcal{L}_2(\gamma_{i,t+1}, \kappa_i^*, G_i; \alpha'_i, \lambda'_i, \eta'_i, \lambda_{i,t}) + \frac{1}{2\tau_{i,t}^m} \|\kappa_{i,t+1}^m - \kappa_{i,t+1}^{m-1}\|^2 \right) \end{aligned}$$

are convergent. Here, $\gamma_i^* \in \Gamma_i^*, \gamma_i^* \in \mathbb{R}_+^{k_i}$, is a solution of the state-inference cost and $\kappa_i^* \in K_i^*, \kappa_i^* \in \mathbb{R}^{d_i}$, is a solution of the cause-inference cost. We have assumed, here, that the state update, for a positive step size $\tau_{i,t}^m \in \mathbb{R}_+$, was given by the relation $\gamma_{i,t+1}^m = \text{PROX}_{\lambda_{i,t}}(\pi_{i,t}^m - \lambda_{i,t} \tau_{i,t}^m \nabla_{\pi_{i,t}^m} \mathcal{L}_1(\pi_{i,t}^m, \kappa_{i,t}, C_i, D_i^\top; \alpha_i, \lambda_{i,t}))$, with the auxiliary update $\pi_{i,t+1}^m = \gamma_{i,t+1}^m + \beta_m(\gamma_{i,t+1}^m - \gamma_{i,t+1}^{m-1})$. As well, the cause update, for a positive step size $\tau'_{i,t} \in \mathbb{R}_+$, was $\kappa_{i,t+1}^m = \text{PROX}_{\lambda'_i}(\pi'_{i,t}^m - \lambda'_i \tau'_{i,t} \nabla_{\pi'_{i,t}^m} \mathcal{L}_2(\gamma_{i,t+1}, \pi'_{i,t}^m, G_i; \alpha'_i, \lambda'_i, \eta'_i, \lambda_{i,t}))$, with the auxiliary cause update $\pi'_{i,t+1}^m = \kappa_{i,t+1}^m + \beta'_m(\kappa_{i,t+1}^m - \kappa_{i,t+1}^{m-1})$.

Proof: For ease of presentation, we ignore the variables of the inference cost that remain fixed across inference iterations. It can be shown that

$$\begin{aligned} & \mathcal{L}_1(\gamma_{i,t+1}^m) - \mathcal{L}_1(\gamma_i^*) + \beta_m^2 \|\gamma_{i,t+1}^m - \gamma_{i,t+1}^{m-1}\|^2/2\tau_{i,t}^m \\ & \geq \mathcal{L}_1(\gamma_{i,t+1}^{m+1}) - \mathcal{L}_1(\gamma_i^*) + \|\gamma_{i,t+1}^m - \gamma_{i,t+1}^{m+1}\|^2/2\tau_{i,t}^{m+1}. \end{aligned}$$

Multiplying both sides by k_{m+1}^2 , performing an addition by zero, and re-arranging terms yields

$$\begin{aligned} & k_{m+1}^3 (\mathcal{L}_1(\gamma_{i,t+1}^m) - \mathcal{L}_1(\gamma_i^*)) + k_{m+1}^3 \|\gamma_{i,t+1}^m - \gamma_{i,t+1}^{m-1}\|^2 / 2\tau_{i,t}^m \\ & \leq (k_{m+1}^3 + k_m^3 - k_m^3) (\mathcal{L}_1(\gamma_{i,t+1}^m) - \mathcal{L}_1(\gamma_i^*)) - k_{m+1} (k_m - 1)^2 \|\gamma_{i,t+1}^m - \gamma_{i,t+1}^{m-1}\|^2 / 2\tau_{i,t}^m \\ & \leq k_m^3 (\mathcal{L}_1(\gamma_{i,t+1}^m) - \mathcal{L}_1(\gamma_i^*)) + k' (\mathcal{L}_1(\gamma_{i,t+1}^m) - \mathcal{L}_1(\gamma_i^*)) - (k_m^2 (2 - k') + k_m (2k' - 1) - k') / 2\tau_{i,t}^m \\ & \quad + k_m^3 \|\gamma_{i,t+1}^m - \gamma_{i,t+1}^{m-1}\|^2 / 2\tau_{i,t}^m. \end{aligned}$$

The last inequality follows because $\sum_{m=1}^{\infty} k_m^{-1}$ is divergent. In this case, there exists some $0 < k' < 2$ such that $k_{m+1} - k_m \leq k'$ for all $m > m'$, $m' > 0$. We therefore have that

$$\begin{aligned} & k' (k_m^2 + k_{m+1}) (\mathcal{L}_1(\gamma_{i,t+1}^m) - \mathcal{L}_1(\gamma_i^*)) \\ & \geq k_{m+1}^3 (\mathcal{L}_1(\gamma_{i,t+1}^{m+1}) - \mathcal{L}_1(\gamma_i^*)) + \|\gamma_{i,t+1}^{m+1} - \gamma_{i,t+1}^m\|^2 / 2\tau_{i,t}^{m+1} + k_m^3 (\mathcal{L}_1(\gamma_{i,t+1}^m) - \mathcal{L}_1(\gamma_i^*)) \\ & \quad + \|\gamma_{i,t+1}^m - \gamma_{i,t+1}^{m-1}\|^2 / 2\tau_{i,t}^m. \end{aligned}$$

Re-organizing terms allows us to demonstrate that $\sum_{m=1}^{\infty} \|\gamma_{i,t+1}^m - \gamma_{i,t+1}^{m-1}\|^2 / 2\tau_{i,t}^m$ is convergent via a Cauchy test. This implies that $\sum_{m=1}^{\infty} k_m^2 (\mathcal{L}_1(\gamma_{i,t+1}^m) - \mathcal{L}_1(\gamma_i^*)) + \|\gamma_{i,t+1}^m - \gamma_{i,t+1}^{m-1}\|^2 / 2\tau_{i,t}^m$ is also convergent. A similar argument to what is above can be used for the causes. ■

The rate of convergence, though, is limited when choosing a Nesterov-style inertial sequence, both locally and globally. In the global case, we have that

Proposition A.5. Let $\gamma_{i,t} \in \mathbb{R}_+^{k_i}$ be the hidden states and $\kappa_{i,t} \in \mathbb{R}^{d_i}$ be the hidden causes. The state iterates $\{\gamma_{i,t+1}^m\}_{m=1}^{\infty}$ strongly converge to the global solution of $\mathcal{L}_1(\gamma_{i,t}, \kappa_{i,t}, C_i, D_i^\top; \alpha_i, \lambda_{i,t})$ for the accelerated proximal gradient scheme. Likewise, the cause iterates $\{\kappa_{i,t+1}^m\}_{m=1}^{\infty}$ for the accelerated proximal gradient scheme strongly converge to the global solution of $\mathcal{L}_2(\gamma_{i,t+1}, \kappa_{i,t}, G_i; \alpha'_i, \lambda'_i, \eta'_i, \lambda_{i,t})$ at a sub-quadratic rate. This occurs when using the inertial sequences $\beta_m, \beta'_m = (k_m - 1) / k_{m+1}$, where $k_{m+1} = (1 + (1 + 4k_m^2)^{1/2}) / 2$.

Proof: Strong convergence of the states $\{\gamma_{i,t+1}^m\}_{m=1}^{\infty}$ and causes $\{\kappa_{i,t+1}^m\}_{m=1}^{\infty}$ to the optimal solutions $\gamma_i^* \in \Gamma_i^*$ and $\kappa_i^* \in K_i^*$ can be obtained from an extension of proposition A.4. For the convergence rate, we note that there is some $\zeta_i \in \mathbb{R}_+$ such that $\zeta_i m^{-3/2} \geq \|\gamma_{i,t+1}^{m-1} - \gamma_{i,t+1}^m\|$. For $m' > 1$, we have that $\|\gamma_{i,t+1}^{m+m'} - \gamma_{i,t+1}^m\|$ is bounded above by $\sum_{j=m+1}^{m+m'} \|\gamma_{i,t+1}^j - \gamma_{i,t+1}^{j-1}\| \leq \zeta_i \sum_{j=m+1}^{m+m'} m^{-3}$. As $m' \rightarrow \infty$, $\|\gamma_{i,t+1}^m - \gamma_i^*\| \leq \zeta_i / 2m^2$, which implies a sub-quadratic rate of convergence for the state and cause iterate sequences. ■

To better understand why the convergence is better with a polynomial inertial sequence, it is helpful to re-cast the proximal gradient updates in a way that permits understanding local convergence behaviors using spectral analysis. We do this first for the state-inference process.

Proposition A.6. The state update $\gamma_{i,t+1}^m = \text{PROX}_{\lambda_{i,t}}(\pi_{i,t}^m - \lambda_{i,t} \tau_{i,t}^m \nabla_{\pi_{i,t}} \mathcal{L}_1(\pi_{i,t}, \kappa_{i,t}, C_i, D_i^\top; \alpha_i, \lambda_{i,t}))$, with $\pi_{i,t}^{m+1} = \gamma_{i,t}^m + \beta_m (\gamma_{i,t}^m - \gamma_{i,t}^{m-1})$, is equivalent to $\gamma_{i,t+1}^m = \text{SHRINK}(w_{i,t}^m; \lambda_{i,t} / \ell_{i,t})$, for the auxiliary variable

$$w_{i,t}^m = \left(I_{k_i \times k_i} - \ell_{i,t}^{-1} D_i^\top D_i \right) \pi_{i,t}^m + \ell_{i,t}^{-1} D_i^\top \kappa_{i-1,t} + \alpha_i \ell_{i,t}^{-1} \text{PROJ}_\infty \left((\pi_{i,t}^m - C_i \gamma_{i,t-1}) / \mu_i \right),$$

where $I_{k_i \times k_i} \in \mathbb{R}_+^{k_i \times k_i}$ is the identity matrix, $0_{1 \times 2k_i} \in \mathbb{R}^{2k_i}$ is a row vector of zeros and $1_{k_i+1 \times 1} \in \mathbb{R}_+^{k_i+1}$ is a column vector of ones. This is equivalent to the homogeneous matrix recurrence

$$\begin{pmatrix} w_{i,t}^{m+1} \\ w_{i,t}^m \\ 1 \end{pmatrix} = \underbrace{\begin{pmatrix} W_{i,t}^m & \ell_{i,t}^{-1} D_i^\top \kappa_{i-1,t} + (I_{k_i \times k_i} - \ell_{i,t}^{-1} D_i^\top D_i) z_{i,t}^m + \alpha_i \ell_{i,t}^{-1} f_{i,t}^m \\ 0_{1 \times 2k_i} & 1_{k_i+1 \times 1} \end{pmatrix}}_{S_{i,t}^m} \begin{pmatrix} w_{i,t}^m \\ w_{i,t}^{m-1} \\ 1 \end{pmatrix}$$

where $z_{i,t}^m = -(1 + \beta_m) \lambda_{i,t} s_{i,t}^m / \ell_{i,t} + \beta_m \lambda_{i,t} s_{i,t}^{m-1} / \ell_{i,t}$, with $s_{i,t}^m = \text{SIGN}(\text{SHRINK}(w_{i,t}^m; \lambda_{i,t} / \ell_{i,t}))$. The term $f_{i,t}^m$ accounts for the Nesterov-smoothed component, $f_{i,t}^m = \text{PROJ}_\infty(((H_{i,t}^m)^2 w_{i,t}^m - \lambda_{i,t} \ell_{i,t}^{-1} s_{i,t}^m - C_i \gamma_{i,t-1}) / \mu_i)$, which is given by projecting the L_1 -sparse state-transition component onto an L_∞ ball. The matrix $W_{i,t}^m \in \mathbb{R}^{2k_i \times 2k_i}$ is

$$W_{i,t}^m = \begin{pmatrix} (1 + \beta_m)(I_{k_i \times k_i} - \ell_{i,t}^{-1} D_i^\top D_i)(H_{i,t}^m)^2 & -\beta_{m+1}(I_{k_i \times k_i} - \ell_{i,t}^{-1} D_i^\top D_i)(H_{i,t}^m)^2 \\ I_{k_i \times k_i} & 0_{k_i \times k_i} \end{pmatrix}.$$

Here, $\ell_{i,t} \in \mathbb{R}_{0,+}$ is the Lipschitz constant of the state-inference cost at a given layer i and for the current batch t . The flag matrix $H_{i,t}^m = \text{DIAG}(\text{SIGN}(\text{SHRINK}(w_{i,t}^m; \lambda_{i,t} / \ell_{i,t})))$ is diagonal and relies on a sparse shrinkage process for the auxiliary variable.

Proof: The underlying update for accelerated proximal gradients can be re-written as

$$\gamma_{i,t+1}^m = \arg \min_{\pi} (\|\pi - (\pi_{i,t}^m - \ell_{i,t}^{-1} \nabla_{\pi_{i,t}} \mathcal{L}_1(\pi_{i,t}))\|^2 / 2\ell_{i,t} + \lambda_{i,t} \|\pi\|_1)$$

$$= \text{SHRINK}((I_{k_i \times k_i} - \ell_{i,t}^{-1} D_i^\top D_i) \pi_{i,t}^m + \ell_{i,t}^{-1} D_i^\top \kappa_{i-1,t} + \alpha_i \ell_{i,t}^{-1} \text{PROJ}_\infty((\pi_{i,t}^m - C_i \gamma_{i,t-1}) / \mu_i); \lambda_{i,t} / \ell_{i,t})$$

where $\mathcal{L}'_1(\pi_{i,t}^m)$ represents the state-inference cost but without the L_1 -sparsity constraint on the states. Here, we have used a Nesterov smoothing approach, with $\mu_i \in \mathbb{R}_+$, to deal with the L_1 -sparse state-transition update, $\arg \max_{\|\Omega_{i,t}\|_\infty \leq 1} \Omega_{i,t}^\top (\pi_{i,t}^m - C_i \gamma_{i,t-1}) - \mu_i \|\Omega_{i,t}\|_2^2 / 2 = \text{PROJ}_\infty((\pi_{i,t}^m - C_i \gamma_{i,t-1}) / \mu_i)$. This projection onto an L_∞ -ball has the closed-form solution

$$\text{PROJ}_\infty((\pi_{i,t}^m - C_i \gamma_{i,t-1}) / \mu_i) = \begin{cases} 1, & (\pi_{i,t}^m - C_i \gamma_{i,t-1}) / \mu_i > 1 \\ (\pi_{i,t}^m - C_i \gamma_{i,t-1}) / \mu_i, & -1 \leq (\pi_{i,t}^m - C_i \gamma_{i,t-1}) / \mu_i \leq 1 \\ -1, & (\pi_{i,t}^m - C_i \gamma_{i,t-1}) / \mu_i < -1 \end{cases}.$$

We replace the states by the auxiliary variable $w_{i,t}^m$ and note that $\gamma_{i,t+1}^m = \text{SHRINK}(w_{i,t}^m; \lambda_{i,t} / \ell_{i,t})$, where

$$\text{SHRINK}(w_{i,t}^m; \lambda_{i,t} / \ell_{i,t}) = \text{DIAG}(\text{SIGN}(\text{SHRINK}(w_{i,t}^m; \lambda_{i,t} / \ell_{i,t})))^2 w_{i,t}^m - \lambda_{i,t} \text{SIGN}(\text{SHRINK}(w_{i,t}^m; \lambda_{i,t} / \ell_{i,t})) / \ell_{i,t},$$

$$\text{SIGN}(\text{SHRINK}(w_{i,t}^m; \lambda_{i,t} / \ell_{i,t})) = \begin{cases} 1, & w_{i,t}^m > \lambda_{i,t} / \ell_{i,t} \\ 0, & -\lambda_{i,t} / \ell_{i,t} \leq w_{i,t}^m \leq \lambda_{i,t} / \ell_{i,t} \\ -1, & w_{i,t}^m < -\lambda_{i,t} / \ell_{i,t} \end{cases}.$$

We can systematically re-write the auxiliary-variable update as

$$\begin{aligned} w_{i,t}^{m+1} &= (I_{k_i \times k_i} - \ell_{i,t}^{-1} D_i^\top D_i) (\gamma_{i,t+1}^m + \beta_m (\gamma_{i,t+1}^m - \gamma_{i,t}^{m-1})) + \ell_{i,t}^{-1} D_i^\top \kappa_{i-1,t} + \alpha_i \ell_{i,t}^{-1} \text{PROJ}_\infty((\gamma_{i,t+1}^m - C_i \gamma_{i,t}) / \mu_i) \\ &= (I_{k_i \times k_i} - \ell_{i,t}^{-1} D_i^\top D_i) ((1 + \beta_m) (H_{i,t}^{m-1})^2 w_{i,t}^m - \lambda_{i,t} \text{SIGN}(\text{SHRINK}(w_{i,t}^{m-1}; \lambda_{i,t} / \ell_{i,t})) / \ell_{i,t}) \\ &\quad - (I_{k_i \times k_i} - \ell_{i,t}^{-1} D_i^\top D_i) (\beta_{m-1} (H_{i,t}^m)^2 w_{i,t}^m + \lambda_{i,t} \text{SIGN}(\text{SHRINK}(w_{i,t}^{m-1}; \lambda_{i,t} / \ell_{i,t})) / \ell_{i,t}) \\ &\quad - \ell_{i,t}^{-1} D_i^\top \kappa_{i-1,t} + \alpha_i \ell_{i,t}^{-1} \text{PROJ}_\infty((\gamma_{i,t+1}^m - C_i \gamma_{i,t}) / \mu_i) \\ &= (1 + \beta_m) (I_{k_i \times k_i} - \ell_{i,t}^{-1} D_i^\top D_i) (H_{i,t}^m)^2 w_{i,t}^m - \beta_m (I_{k_i \times k_i} - \ell_{i,t}^{-1} D_i^\top D_i) (H_{i,t}^{m-1})^2 w_{i,t}^{m-1} - \ell_{i,t}^{-1} D_i^\top \kappa_{i-1,t} \\ &\quad + (I_{k_i \times k_i} - \ell_{i,t}^{-1} D_i^\top D_i) ((-\lambda_{i,t} - \lambda_{i,t} \beta_m) \text{SIGN}(\text{SHRINK}(w_{i,t}^{m-1}; \lambda_{i,t} / \ell_{i,t})) / \ell_{i,t} \\ &\quad + \lambda_{i,t} \beta_m) \text{SIGN}(\text{SHRINK}(w_{i,t}^{m-1}; \lambda_{i,t} / \ell_{i,t})) / \ell_{i,t} + \alpha_i \ell_{i,t}^{-1} \text{PROJ}_\infty((\gamma_{i,t+1}^m - C_i \gamma_{i,t}) / \mu_i). \end{aligned}$$

The matrix recurrence follows from this update. ■

We now characterize the cause inference in a similar manner.

Proposition A.7. The cause update $\kappa_{i,t+1}^m = \text{PROX}_{\lambda_i}(\pi_{i,t}^m - \lambda'_i \tau_{i,t}^m \nabla \pi_{i,t}^m \mathcal{L}_2(\gamma_{i,t+1}, \pi_{i,t}^m, G_i; \alpha'_i, \lambda'_i, \eta'_i, \lambda_{i,t}))$, with $\pi_{i,t}^{m+1} = \kappa_{i,t+1}^m + \beta'_m (\kappa_{i,t+1}^m - \kappa_{i,t}^m)$, is equivalent to $\kappa_{i,t+1}^m = \text{SHRINK}(v_{i,t}^m; \lambda'_i / \ell'_{i,t})$, for the auxiliary variable

$$v_{i,t}^m = \left(I_{d_i \times d_i} - 1 / \ell'_{i,t} \right) \pi_{i,t}^m + 2\eta'_i I_{d_i \times d_i} \kappa'_{i,t} / \ell'_{i,t} - \alpha'_i / \ell'_{i,t} \left(G_i^\top \exp(-G_i \pi_{i,t}^m) |\gamma_{i,t+1}^j| \right),$$

where $I_{d_i \times d_i} \in \mathbb{R}_+^{d_i \times d_i}$ is the identity matrix, $0_{1 \times 2d_i} \in \mathbb{R}^{2d_i}$ is a row vector of zeros and $1_{d_i+1 \times 1} \in \mathbb{R}_+^{d_i+1}$ is a column vector of ones. This is equivalent to the homogeneous matrix recurrence

$$\begin{pmatrix} v_{i,t}^{m+1} \\ v_{i,t}^m \\ 1 \end{pmatrix} = \underbrace{\begin{pmatrix} V_{i,t}^m & 2\eta'_i I_{d_i \times d_i} \kappa'_{i,t} / \ell'_{i,t} + (I_{d_i \times d_i} - 1 / \ell'_{i,t}) z_{i,t}^m - \alpha'_i g_{i,t}^m / \ell'_{i,t} \\ 0_{1 \times 2d_i} & 1_{d_i+1 \times 1} \end{pmatrix}}_{T_{i,t}^m} \begin{pmatrix} v_{i,t}^m \\ v_{i,t}^{m-1} \\ 1 \end{pmatrix}$$

where $z_{i,t}^m = -(1 + \beta'_m) \lambda'_i q_{i,t}^m / \ell'_{i,t} + \beta'_m \lambda'_i q_{i,t}^{m-1} / \ell'_{i,t}$, with $q_{i,t}^m = \text{SIGN}(\text{SHRINK}(v_{i,t}^m; \lambda'_i / \ell'_{i,t}))$. The term $g_{i,t}^m$ accounts for the invariant-matrix component, $g_{i,t}^m = G_i^\top \exp(-G_i v_{i,t}^m) |\gamma_{i,t+1}^j|$. The matrix $V_{i,t}^m \in \mathbb{R}^{2d_i \times 2d_i}$ is

$$V_{i,t}^m = \begin{pmatrix} (1 + \beta'_m) (I_{d_i \times d_i} - 1 / \ell'_{i,t}) (M_{i,t}^m)^2 & -\beta'_{m+1} (I_{d_i \times d_i} - 1 / \ell'_{i,t}) (M_{i,t}^m)^2 \\ I_{d_i \times d_i} & 0_{d_i \times d_i} \end{pmatrix}.$$

Here, $\ell'_{i,t} \in \mathbb{R}_{0,+}$ is the Lipschitz constant of the state-inference cost at a given layer i and for the current batch t . The flag matrix $M_{i,t}^m = \text{DIAG}(\text{SIGN}(\text{SHRINK}(v_{i,t}^m; \lambda'_i / \ell'_{i,t})))$ is diagonal and relies on a sparse shrinkage process for the auxiliary variable.

We now list spectral properties of the iteration matrices $W_{i,t}^m \in \mathbb{R}^{k_i+1 \times k_i+1}$ and $V_{i,t}^m \in \mathbb{R}^{d_i+1 \times d_i+1}$. The validity of these claims follows from extensions of the work in [3].

Lemma A.1. Suppose that the flag matrices across consecutive iterations m of the hidden state and cause updates respectively satisfy $H_{i,t}^{m-1} = H_{i,t}^m = H_{i,t}^{m+1}$ and $M_{i,t}^{m-1} = M_{i,t}^m = M_{i,t}^{m+1}$. The iteration matrices $W_{i,t}^m$ and $V_{i,t}^m$ are different at each step and satisfy:

- (i) $\|W_{i,t}^m\|_2 \leq 1$ and $\|V_{i,t}^m\|_2 \leq 1$. Also, $\|(I_{k_i \times k_i} - \ell_{i,t}^{-1} D_i^\top D_i) H_{i,t}^m\|_2 \leq 1$ and $\|(I_{d_i \times d_i} - 1/\ell'_{i,t}) M_{i,t}^m\|_2 \leq 1$.
- (ii) For any $0 < \beta_m, \beta'_m \leq 1$, the eigenvalues of $W_{i,t}^m$ and $V_{i,t}^m$ lie in a closed circle in the real-complex plane that is centered at $(0, \frac{1}{2})$ and that has a radius of $\frac{1}{2}$. If either of these iteration matrices has eigenvalues with absolute values of $\rho(W_{i,t}^m) = 1$ and $\rho(V_{i,t}^m) = 1$, then there must be no imaginary component. If the step sizes are such that $\beta_m, \beta'_m < 1$ and if $W_{i,t}^m$ and $V_{i,t}^m$ have eigenvalues of one, then these eigenvalues must have a complete set of eigenvectors.

Now, suppose that the flag matrices $H_{i,t}^m$ and $M_{i,t}^m$ are such that they are not necessarily equal across iterations m . The full iteration matrices have spectral decompositions $S_{i,t}^m = P_{i,t}^m J_{i,t}^m (P_{i,t}^m)^{-1}$ and $T_{i,t}^m = Q_{i,t}^m R_{i,t}^m (Q_{i,t}^m)^{-1}$ where the block-diagonal eigenvalue matrices $J_{i,t}^m$ and $R_{i,t}^m$ have the form

$$J_{i,t}^m = \begin{pmatrix} \begin{pmatrix} 1 & 1 \\ 0 & 1 \end{pmatrix} & 0 & 0 \\ 0 & I_{i,t}^m & 0 \\ 0 & 0 & J_{i,t}'^m \end{pmatrix}, \quad R_{i,t}^m = \begin{pmatrix} \begin{pmatrix} 1 & 1 \\ 0 & 1 \end{pmatrix} & 0 & 0 \\ 0 & I_{i,t}^m & 0 \\ 0 & 0 & R_{i,t}'^m \end{pmatrix},$$

where $I_{i,t}^m$ is an appropriately sized identity matrix that will depend on the flag matrix at iteration m for layer i and batch t . Here, we have the condition that the spectral radii $\rho(J_{i,t}^m) < 1$ and $\rho(R_{i,t}^m) < 1$. Some of these blocks may be missing depending on either the equivalency or non-equivalency of the flag matrices across iterations.

This lemma suggests that there are multiple local phases that can arise from matrix-based proximal-gradient recurrence. These phases depend on properties of the flag matrix on the spectral characteristics of the full iteration matrices that define the matrix recurrence. If the flag matrices remain the same across consecutive iterations, then the total-iteration-matrix operator remains invariant. The structure of the spectrum for that operator controls the convergence behavior of the process. If the flag matrix changes, then the set of active constraints at the current pass in the process has changed across consecutive iterations. The current iteration is thus a transition to a different operator with a different eigenstructure. The algorithm hence adopts a combinatorial aspect while it searches for the correct set of active constraints. The specific phases are distinguished by the eigenstructure of the total-iteration-matrix operator.

Proposition A.8. Suppose that the flag matrices across consecutive iterations m of the hidden state and cause updates respectively satisfy $H_{i,t}^{m-1} = H_{i,t}^m$ and $M_{i,t}^{m-1} = M_{i,t}^m$. Let the eigendecompositions of the total-iteration matrices be such that $S_{i,t}^m = P_{i,t}^m J_{i,t}^m (P_{i,t}^m)^{-1}$ and $T_{i,t}^m = Q_{i,t}^m R_{i,t}^m (Q_{i,t}^m)^{-1}$, where $J_{i,t}^m$ and $R_{i,t}^m$ have block-diagonal forms. Then, the iterates can belong to one of the following phases:

(i) Let the spectral radii $\rho(W_{i,t}^m) < 1$ and $\rho(V_{i,t}^m) < 1$. In this case, the $\mathbb{R}_{0,+}^{2 \times 2}$ Jordan blocks in the upper-left corners of the eigenvalue matrices $J_{i,t}^m$ and $R_{i,t}^m$ are not present. The identity-matrix blocks $I_{i,t}^m \in \mathbb{R}_+^{1 \times 1}$ are degenerate. As long as the flag matrices $H_{i,t}^m$ and $M_{i,t}^m$ do not change across m and if the iterates are close enough to the optimal solution, then linear convergence is achieved to that solution. Such solutions are unique fixed points which are eigenvectors $[P_{i,t}^m]_{1:2k_i+1, 2k_i+1}$ and $[Q_{i,t}^m]_{1:2d_i+1, 2d_i+1}$ of $S_{i,t}^m$ and $T_{i,t}^m$ with unit eigenvalues. If the eigenvectors are non-negative, then they satisfy the Karush-Kuhn-Tucker conditions for the state and cause inference costs.

(ii) If $\rho(W_{i,t}^m) = 1$ and $\rho(V_{i,t}^m) = 1$, then $S_{i,t}^m$ and $T_{i,t}^m$ both have non-trivial $\mathbb{R}_{0,+}^{2 \times 2}$ Jordan blocks in the upper-left corners of $J_{i,t}^m$ and $R_{i,t}^m$. There are no other eigenvalues on the unit circle. The theory of the power method implies that the vector iterates will converge to an invariant subspace corresponding to the unit eigenvalue. The presence of the non-trivial Jordan block implies the existence of a Jordan chain. That is, there are non-zero vectors $\varphi, \varphi' \in \mathbb{R}_{0,+}^{2k_i+1}$ and $\phi, \phi' \in \mathbb{R}_{0,+}^{2d_i+1}$ such that the equivalence relations $(S_{i,t}^m - I_{2k_i+1, 2k_i+1})\varphi = \varphi'$ and $(S_{i,t}^m - I_{2k_i+1, 2k_i+1})\varphi' = 0$ along with $(T_{i,t}^m - I_{2d_i+1, 2d_i+1})\phi = \phi'$ and $(T_{i,t}^m - I_{2d_i+1, 2d_i+1})\phi' = 0$ are satisfied. Any vector that includes a component of the form $a\varphi + b\varphi'$ and $a\phi + b\phi'$, for $a, b \in \mathbb{R}$ would add a constant factor $a\varphi$ and $a\phi$, respectively, to $S_{i,t}^m$ and $T_{i,t}^m$, plus descending lower-order terms from the other lesser eigenvalues. If $H_{i,t}^m$ and $M_{i,t}^m$ do not change across m , then the state $w_{i,t}^m$ and cause $v_{i,t}^m$ iterates take constant-sized steps and either diverge or drive some component negative, which results in a change in the iteration matrices $W_{i,t}^m$ and $V_{i,t}^m$.

(iii) Suppose that $\rho(W_{i,t}^m) = 1$ and $\rho(V_{i,t}^m) = 1$, but $S_{i,t}^m$ and $T_{i,t}^m$ have no non-diagonal Jordan block for that eigenvalue. If we assume that the solution is unique, then the unit eigenvalues of $S_{i,t}^m$ and $T_{i,t}^m$ must be simple. There are no other eigenvalues on the unit circle. If the iterates are close enough to the optimal solution, then they linearly converge to it, as the inference process behaves similarly to a Von Mises iteration. These unique, fixed-point solutions are, by definition, the eigenvectors $[P_{i,t}^m]_{1:2k_i+1, 2k_i+1}$ and $[Q_{i,t}^m]_{1:2d_i+1, 2d_i+1}$ of $S_{i,t}^m$ and $T_{i,t}^m$ for the unit eigenvalues. The convergence rate is determined by the next-largest eigenvalues in the absolute value, that is, the largest eigenvalues of $J_{i,t}^m$ and $R_{i,t}^m$, as long as the flag matrices $H_{i,t}^m$ and $M_{i,t}^m$ do not change across m . This phase cannot be last in the inference process, as the search will eventually jump to a different one due to the eigenvalue properties.

Now, suppose that $H_{i,t}^{m-1} \neq H_{i,t}^m$ and $M_{i,t}^{m-1} \neq M_{i,t}^m$ for iterations m . In this case, the iteration operator does not remain invariant over more than one pass. The iteration matrices $W_{i,t}^m$ and $V_{i,t}^m$ could match one of the conditions in the above phases. They could also have the following eigenstructure associated with a fourth phase:

(iv) $W_{i,t}^m$ and $V_{i,t}^m$ have eigenvalues with absolute value one, but not equal to one. This occurs when the iterates transition to a new set of active constraints. The next pass will result in a different operator with a different flag matrix.

Proof: For $S_{i,t}^m$, the upper-left portion, $W_{i,t}^m$, contributes to the eigenvalue blocks $I_{i,t}^m$ and $J_{i,t}^m$ of $J_{i,t}^m$, where $S_{i,t}^m = P_{i,t}^m J_{i,t}^m (P_{i,t}^m)^{-1}$. Both $W_{i,t}^m$ and $S_{i,t}^m$ have the same set of eigenvalues with equivalent geometric and algebraic multiplicities, except when an eigenvalue has an absolute value of one. No eigenvalue with an absolute value of one can have a non-diagonal Jordan block. Hence, the blocks, $I_{i,t}^m$ and $J_{i,t}^m$, corresponding to those eigenvalues must be diagonal.

If $W_{i,t}^m$ has no eigenvalue equal to one, then $S_{i,t}^m$ has a simple eigenvalue that is one. In this case, the algebraic multiplicity increases by one. The geometric multiplicity either increases by one or stays the same.

■

Such results indicate that there are local search regimes in the inference process where the convergence is quicker than the global convergence rate. We can specify the conditions when this will occur.

Proposition A.8. Let the state and cause inference recurrences be defined as in propositions A.6 and A.7, respectively, for the accelerated proximal gradient search. For a non-accelerated search, they become

$$\begin{pmatrix} w_{i,t}^{m+1} \\ 1 \end{pmatrix} = \begin{pmatrix} W_{i,t}^m & \ell_{i,t} D_i^\top \kappa_{i-1,t} - \lambda_{i,t} \ell_{i,t}^{-1} (I_{k_i \times k_i} - \ell_{i,t}^{-1} D_i^\top D_i) s'_{i,t} + \alpha_i \ell_{i,t} f_{i,t}^m \\ 0 & 1 \end{pmatrix} \begin{pmatrix} w_{i,t}^{m+1} \\ 1 \end{pmatrix}$$

where $W_{i,t}^m = (I_{k_i \times k_i} - \ell_{i,t}^{-1} D_i^\top D_i) (H_{i,t}^m)^2$ and $s'_{i,t} = \text{SIGN}(\text{SHRINK}(w_{i,t}^m; \lambda_{i,t}/\ell_{i,t}))$. The flag matrix is such that $H_{i,t}^m = \text{DIAG}(s'_{i,t})$. For the non-accelerated cause inference, we have the recurrence relation

$$\begin{pmatrix} v_{i,t}^{m+1} \\ 1 \end{pmatrix} = \begin{pmatrix} V_{i,t}^m & 2\eta_i' I_{d_i \times d_i} \kappa'_{i,t}/\ell'_{i,t} + (I_{d_i \times d_i} - 1/\ell'_{i,t}) q'_{i,t} - \alpha_i' g'_{i,t}/\ell'_{i,t} \\ 0 & 1 \end{pmatrix} \begin{pmatrix} v_{i,t}^{m+1} \\ 1 \end{pmatrix}$$

where $V_{i,t}^m = (I_{d_i \times d_i} - 1/\ell'_{i,t}) (M_{i,t}^m)^2$ and $q'_{i,t} = \text{SIGN}(\text{SHRINK}(v_{i,t}^m; \lambda_i/\ell'_{i,t}))$. The flag matrix is such that $M_{i,t}^m = \text{DIAG}(q'_{i,t})$. We have that:

(i) For the second phase, the constant step-size vector has the form $(1 - \beta_m)^{-1}(\varphi, \varphi, 0)^\top$, $W_{i,t}^m \varphi = \varphi$, with $\varphi \in \mathbb{R}^{k_i}$ being a scaled eigenvector of the state-inference total-iteration matrix. Likewise, for the cause inference, the constant step-size vector has the form $(1 - \beta'_m)^{-1}(\phi, \phi, 0)^\top$, where $V_{i,t}^m \phi = \phi$, with $\phi \in \mathbb{R}^{d_i}$ being a scaled eigenvector. Since β_m, β'_m have a limit of one, the constant-step-size vector is larger than the one for the states, $(\varphi', 0)$, $W_{i,t}^m \varphi' = \varphi'$, in the non-accelerated proximal-gradient case. The constant-step-size vector in the accelerated case is also larger than the one for the causes, $(\phi', 0)$, $V_{i,t}^m \phi' = \phi'$, in the case of non-accelerated proximal gradients.

(ii) In the first and third phases, if $1 > \rho(W_{i,t}^m) > \beta_m$ and $1 > \rho(V_{i,t}^m) > \beta'_m$, then the accelerated proximal gradient scheme will be faster than the non-accelerated case for the state and cause inference. It will be slower, however, if $1 > \beta_m > \rho(W_{i,t}^m)$ and $1 > \beta'_m > \rho(V_{i,t}^m)$. When $\beta_m > \rho(W_{i,t}^m)$ and $\beta'_m > \rho(V_{i,t}^m)$, then the largest eigenvalues of $W_{i,t}^m$ and $V_{i,t}^m$ must be a pair of complex conjugates. According to the theory of Von Mises iterations, the convergence will oscillate between the two complex numbers and the search will not be monotonically decreasing across iterations. The accelerated case will hence be slower than the non-accelerated case, as $\rho(W_{i,t}^m)$ and $\rho(V_{i,t}^m)$ will remain fixed for a specific phase, while the steps β_m and β'_m will monotonically increase.

Proof: For part (i), a single update has the form $(w_{i,t}^{m+1}, w_{i,t}^m, 1)^\top + (\varphi_1, \varphi_2, 0)^\top$. There exists a Jordan block in $J_{i,t}^m$ and hence a Jordan chain. Therefore, $(S_{i,t}^m - I_{2k_i+1 \times 2k_i+1})(w_{i,t}^{m+1}, w_{i,t}^m, 1)^\top = (\varphi_1, \varphi_2, 0)^\top$ and $S_{i,t}^m(\varphi_1, \varphi_2, 0)^\top = (\varphi_1, \varphi_2, 0)^\top$. It can be seen that $\varphi_1 = \varphi_2$. This implies $W_{i,t}^m \varphi = \varphi$ for the accelerated case. Moreover,

$$(S_{i,t}^m - I_{2k_i+1 \times 2k_i+1}) \begin{pmatrix} w_{i,t}^{m+1} \\ w_{i,t}^m \\ 1 \end{pmatrix} = \begin{pmatrix} ((1 + \beta_m)W_{i,t}^m - I_{k_i \times k_i})w_{i,t}^m - \beta_m W_{i,t}^m w_{i,t}^{m-1} + (I_{k_i \times k_i} - \ell_{i,t}^{-1} D_i^\top D_i)z_{i,t}^m \\ w_{i,t}^m - w_{i,t}^{m-1} \\ 0 \end{pmatrix}$$

where $(S_{i,t}^m - I_{2k_i+1 \times 2k_i+1})(w_{i,t}^{m+1}, w_{i,t}^m, 1)^\top = (1 - \beta_m)^{-1}(\varphi, \varphi, 0)^\top$. For this to occur, we must have that $w_{i,t}^{m-1} = w_{i,t}^m + (\beta_m - 1)^{-1}\varphi$. Similar arguments apply to the causes. The analysis is similar for the non-accelerated proximal-gradient case.

For part (ii), we prove properties for the states and note that they extend to the causes with few changes. Let

$(v_1, v_2)^\top$ be an eigenvector of $W_{i,t}^m$. We have that

$$W_{i,t}^m(v_1, v_2)^\top = \begin{pmatrix} (1 + \beta_m)\rho(W_{i,t}^m)v_2 + \beta_m(I_{k_i \times k_i} - \ell_{i,t}D_i^\top D_i)(H_{i,t}^m)^2 v_2 \\ v_2 \end{pmatrix} = \rho(W_{i,t}^m) \begin{pmatrix} \rho(W_{i,t}^m)v_2 \\ v_2 \end{pmatrix}$$

since $v_1 = \rho(W_{i,t}^m)v_2$. Hence, $(I_{k_i \times k_i} - \ell_{i,t}D_i^\top D_i)(H_{i,t}^m)^2 v_2 = \rho(W_{i,t}^m)^2 v_2 / ((1 + \beta_m)\rho(W_{i,t}^m) - \beta_m)$. This implies that $\rho(W_{i,t}^m)^2 + \beta_m \rho(W_{i,t}^m) - (1 + \beta_m)\rho(W_{i,t}^m)\rho(W_{i,t}^m) = 0$, where $W_{i,t}^m = (I_{k_i \times k_i} - \ell_{i,t}D_i^\top D_i)(H_{i,t}^m)^2$. It can be seen that $\rho(W_{i,t}^m)$ has real-valued roots if $4\beta_m(1 + \beta_m)^2 < \rho(W_{i,t}^m)$ and complex-valued roots otherwise. When there are real-valued roots, then $\rho(W_{i,t}^m) > \beta_m$. Moreover, $\rho(W_{i,t}^m) = (1 + \beta_m)\rho(W_{i,t}^m)/2 + ((1 + \beta_m)^2 \rho(W_{i,t}^m)^2 / 4 - \beta_m \rho(W_{i,t}^m))^{1/2} < \rho(W_{i,t}^m)$, which follows from the fact that $\beta_m < 1$ as per its definition. When there are complex-valued roots, then $|\rho(W_{i,t}^m)| = (\beta_m \rho(W_{i,t}^m))^{1/2}$ and hence $|\rho(W_{i,t}^m)| < \rho(W_{i,t}^m)$ whenever $\rho(W_{i,t}^m) > \beta_m$. If, however, $\beta_m > \rho(W_{i,t}^m)$, then $|\rho(W_{i,t}^m)| > \rho(W_{i,t}^m)$.

Both the accelerated and non-accelerated proximal gradients reduce to a Von Mises iteration in the first and third phases. The rate of convergence is, respectively, determined by $|\rho(W_{i,t}^m)|$ and $|\rho(W_{i,t}^m)|$. ■

This result provides insight into why a Nesterov-style inertial sequence is worse than the one that we employed. It is trivial to demonstrate that the step sizes for a Nesterov inertial sequence will be strictly greater than the step sizes for our polynomial inertial sequence. The former will reach the eigenvalue/step-size inequality conditions more quickly, yielding an inference slowdown whenever the search is in either the first or third phase. Such phases typically occur near the end of the inference process and occupy a majority of the overall process. Moreover, severe cost rippling will be encountered due to the emergence of complex-conjugate eigenvalues in the iteration matrices. Our inertial sequence will likely never reach this point, though, since the search is terminated after only a few hundred steps. If it is reached, then it will occur far later than in the Nesterov case, allowing our accelerated strategy to take advantage of the faster linear convergence for a greater number of iterations.

Although there is a chance that a non-accelerated proximal gradient scheme can locally converge more quickly than ours, this will rarely occur in practice. We often terminate the search process well before it can happen.

References

- [1] Z.-Q. Luo and P. Tseng, "Error bound and convergence analysis of matrix splitting algorithms for the affine variational inequality problem," *SIAM Journal on Optimization*, vol. 2, no. 1, pp. 43–54, 1992. Available: <http://dx.doi.org/10.1137/0802004>
- [2] J.-S. Pang, "A posteriori error bounds for the linearly-constrained variational inequality problem," *Mathematics of Operations Research*, vol. 12, no. 3, pp. 474–484, 1987. Available: <http://dx.doi.org/10.1287/moor.12.3.474>
- [3] D. Boley, "Local linear convergence of the alternating direction method of multipliers on quadratic or linear problems," *SIAM Journal on Optimization*, vol. 23, no. 4, pp. 2183–2207, 2013. Available: <http://dx.doi.org/10.1137/120878951>

Appendix B

Below, we report performance errors for the MNIST, FMNIST, CIFAR-10, CIFAR-100, and STL-10 datasets. For each of the referenced methods, we either report the test-set classification errors that the authors listed or report the best known test-set classification errors obtained using that approach. We also specify whether the chosen approaches were predominantly unsupervised, semi-supervised, or supervised. The best methods for each learning category are highlighted in green. The worst are highlighted in red.

MNIST Error Rate Comparison			FMNIST Error Rate Comparison			CIFAR-10 Error Rate Comparison		
Method	Learning Style	Error	Method	Learning Style	Error	Method	Learning Style	Error
DPCN [1]	Unsupervised	36.2%	DPCN [1]	Unsupervised	42.7%	DPCN [1]	Unsupervised	68.5%
AE [2]	Unsupervised	18.8%	kSCN [12]	Unsupervised	39.9%	NOMP [21]	Unsupervised	39.2%
GAN [3]	Unsupervised	17.2%	CRPN [4]	Unsupervised	8.59%	CRPN [4]	Unsupervised	32.7%
CRPN [4]	Unsupervised	12.6%	ADPCN	Unsupervised	2.51%	RFL [22]	Unsupervised	16.9%
IMSAT [5]	Unsupervised	1.60%	TLML [13]	Semi-super.	11.2%	ADPCN	Unsupervised	7.73%
IIC [6]	Unsupervised	1.60%	ZSDA [14]	Supervised	15.5%	MON [9]	Supervised	9.38%
SCAE [7]	Unsupervised	1.00%	DAGH [15]	Supervised	6.30%	DASN [23]	Supervised	9.22%
EBSR [8]	Unsupervised	0.39%	DCAP [16]	Supervised	5.54%	ACN [24]	Supervised	9.08%
ADPCN	Unsupervised	0.31%	DRBC [17]	Supervised	4.30%	SPNET [25]	Supervised	8.60%
MON [9]	Supervised	0.45%	DNET [18]	Supervised	4.60%	HNET [26]	Supervised	7.69%
RCNN [10]	Supervised	0.31%	LES [19]	Supervised	4.14%	LAF [27]	Supervised	7.51%
MCNN [11]	Supervised	0.23%	JOUT [20]	Supervised	2.87%	RCNN [10]	Supervised	7.09%

CIFAR-100 Error Rate Comparison			STL-10 Error Rate Comparison		
Method	Learning Style	Error	Method	Learning Style	Error
DPCN [1]	Unsupervised	95.6%	DPCN [1]	Unsupervised	87.1%
AEVB [28]	Unsupervised	84.8%	SWAE [36]	Unsupervised	72.9%
DEC [29]	Unsupervised	81.5%	JULE [37]	Unsupervised	72.3%
DAIC [30]	Unsupervised	76.2%	DCNN [38]	Unsupervised	70.1%
DCCM [31]	Unsupervised	67.3%	DEC [29]	Unsupervised	64.1%
CRPN [4]	Unsupervised	59.7%	CRPN [4]	Unsupervised	55.5%
ADPCN	Unsupervised	29.7%	SRF [39]	Unsupervised	39.9%
PMO [32]	Supervised	38.1%	ADPCN	Unsupervised	17.3%
TREE [33]	Supervised	36.8%	CKN [40]	Supervised	37.6%
SBO [34]	Supervised	27.4%	MTBO [41]	Supervised	29.9%
INIT [35]	Supervised	26.3%	SSTN [42]	Supervised	23.4%
DNET [18]	Supervised	17.1%	RESN [43]	Supervised	14.2%

References

- [1] J. C. Príncipe and R. Chalasani, “Cognitive architectures for sensory processing,” *Proceedings of the IEEE*, vol. 102, no. 4, pp. 514–525, 2014. Available: <http://dx.doi.org/10.1109/JPROC.2014.2307023>
- [2] Y. Bengio, P. Lamblin, D. Popovici, and J. Larochelle, “Greedy layer-wise training of deep networks,” in *Advances in Neural Information Processing Systems (NIPS)*, B. Schölkopf, J. C. Platt, and T. Hoffman, Eds. Cambridge, MA, USA: MIT Press, 2007, pp. 153–160.
- [3] A. Radford, L. Metz, and S. Chintala, “Unsupervised representation learning with deep convolutional generative adversarial networks,” in *Proceedings of the International Conference on Learning Representations (ICLR)*, San Juan, Puerto Rico, May 2–4 2016, pp. 1–16. Available: <https://arxiv.org/abs/1511.06434>
- [4] R. Chalasani and J. C. Príncipe, “Context dependent encoding using convolutional dynamic networks,” *IEEE Transactions on Neural Networks and Learning Systems*, vol. 26, no. 9, pp. 1992–2004, 2015. Available: <http://dx.doi.org/10.1109/TNNLS.2014.2360060>
- [5] W. Hu, T. Miyato, S. Tokui, E. Matsumoto, and M. Sugiyama, “Learning discrete representations via information maximizing self-augmented training,” in *Proceedings of the International Conference on Machine Learning (ICML)*, Sydney, Australia, August 6–11 2017, pp. 1558–1567. Available: <http://dx.doi.org/10.5555/3305381.3305542>
- [6] X. Ji, A. Vedaldi, and J. Henriques, “Invariant information clustering for unsupervised image classification and segmentation,” in *Proceedings of the IEEE International Conference on Computer Vision (ICCV)*, Seoul, South Korea, October 27–November 2 2019, pp. 9864–9873. Available: <http://dx.doi.org/DOI:10.1109/ICCV.2019.00996>
- [7] A. Kosiorek, S. Sabour, Y. W. Teh, and G. E. Hinton, “Stacked capsule autoencoders,” in *Advances in Neural Information Processing Systems (NIPS)*, H. Wallach, H. Larochelle, A. Beygelzimer, F. d’Alché-Buc, E. Fox, and R. Garnett, Eds. Red Hook, NY, USA: Curran Associates, 2019, pp. 15 512–15 522.
- [8] M. Ranzato, C. Poultney, S. Chopra, and Y. LeCun, “Efficient learning of sparse representations with an energy-based model,” in *Advances in Neural Information Processing Systems (NIPS)*, B. Schölkopf, J. C. Platt, and T. Hoffman, Eds. Cambridge, MA, USA: MIT Press, 2007, pp. 1137–1144.

- [9] I. J. Goodfellow, D. Warde-Farley, M. Mirza, A. Courville, and Y. Bengio, "Maxout networks," in *Proceedings of the International Conference on Machine Learning (ICML)*, Atlanta, GA, USA, June 16-21 2013, pp. 1319–1327. Available: <http://dx.doi.org/10.5555/3042817.3043084>
- [10] M. Liang and X. Hu, "Recurrent convolutional neural network for object recognition," in *Proceedings of the IEEE International Conference on Computer Vision and Pattern Recognition (CVPR)*, Boston, MA, USA, June 7-12 2015, pp. 3367–3375. Available: <http://dx.doi.org/10.1109/CVPR.2015.7298958>
- [11] D. Ciregan, U. Meier, and J. Schmidhuber, "Multi-column deep neural networks for image classification," in *Proceedings of the IEEE International Conference on Computer Vision and Pattern Recognition (CVPR)*, Providence, RI, USA, June 16-21 2012, pp. 3642–3649. Available: <http://dx.doi.org/10.1109/CVPR.2012.6248110>
- [12] T. Zhang, P. Ji, M. Harandi, R. Hartley, and I. Reid, "Scalable deep k -subspace clustering," in *Proceedings of the Asian Conference on Computer Vision (ACCV)*, Perth, Australia, December 2-6 2018, pp. 466–481. Available: <http://dx.doi.org/10.1109/10.1007/978-3-030-20873-8>
- [13] B. Yu, T. Liu, M. Gong, C. Ding, and D. Tao, "Correcting the triplet selection bias for triplet loss," in *Proceedings of the European Conference on Computer Vision (ECCV)*, Munich, Germany, September 8-14 2018, pp. 71–86. Available: <http://dx.doi.org/10.1007/978-3-030-01231-1>
- [14] K.-C. Peng, Z. Wu, and J. Ernst, "Zero-shot deep domain adaptation," in *Proceedings of the European Conference on Computer Vision (ECCV)*, Munich, Germany, September 8-14 2018, pp. 793–810. Available: <http://dx.doi.org/10.1007/978-3-030-01252-6>
- [15] Y. Chen, Z. Lai, Y. Ding, L. Lin, and W. Wong, "Deep supervised hashing with anchor graph," in *Proceedings of the IEEE International Conference on Computer Vision (ICCV)*, Seoul, South Korea, October 27-November 2 2019, pp. 9795–9803. Available: <http://dx.doi.org/10.1109/ICCV.2019.00989>
- [16] J. Rajasegaran, V. Jayasundara, S. Jayasekara, H. Jayasekara, S. Seneviratne, and R. Rodrigo, "DeepCaps: Going deeper with capsule networks," in *Proceedings of the IEEE International Conference on Computer Vision and Pattern Recognition (CVPR)*, Long Beach, CA, USA, June 15-20 2019, pp. 10 717–10 725. Available: <http://dx.doi.org/10.1109/CVPR.2019.01098>
- [17] S. Sabour, N. Frosst, and G. E. Hinton, "Dynamic routing between capsules," in *Advances in Neural Information Processing Systems (NIPS)*, I. Guyon, U. V. Luxburg, S. Bengio, H. Wallach, R. Fergus, S. Vishwanathan, and R. Garnett, Eds. Red Hook, NY, USA: Curran Associates, 2017, pp. 3856–3866.
- [18] G. Huang, Z. Liu, L. van der Maaten, and K. Q. Weinberger, "Densely connected convolutional networks," in *Proceedings of the IEEE International Conference on Computer Vision and Pattern Recognition (CVPR)*, Honolulu, HI, USA, July 21-26 2017, pp. 2261–2269. Available: <http://dx.doi.org/10.1109/CVPR.2017.243>
- [19] A. Nøkland and L. H. Eidnes, "Training neural networks with local error signals," in *Proceedings of the International Conference on Machine Learning (ICML)*, Long Beach, CA, USA, June 10-15 2019, pp. 4839–4850.
- [20] S. Wang, T. Zhou, and J. Bilmes, "Jumpout: Improved dropout for deep neural networks with ReLUs," in *Proceedings of the International Conference on Machine Learning (ICML)*, Long Beach, CA, USA, June 10-15 2019, pp. 6668–6676.
- [21] T.-H. Lin and H. T. Kung, "Stable and efficient representation learning with nonnegativity constraints," in *Proceedings of the International Conference on Machine Learning (ICML)*, Beijing, China, June 22-24 2014, pp. 1323–1331.
- [22] Y. Jia, C. Huang, and T. Darrell, "Beyond spatial pyramids: Receptive field learning for pooled image features," in *Proceedings of the IEEE International Conference on Computer Vision and Pattern Recognition (CVPR)*, Providence, RI, USA, June 16-21 2012, pp. 3370–3377. Available: <http://dx.doi.org/10.1109/CVPR.2012.6248076>
- [23] M. F. Stollenga, J. Masci, F. Gomez, and J. Schmidhuber, "Deep networks with internal selective attention through feedback connections," in *Advances in Neural Information Processing Systems (NIPS)*, Z. Ghahramani, M. Welling, C. Cortes, N. D. Lawrence, and K. Q. Weinberger, Eds. Red Hook, NY, USA: Curran Associates, 2014, pp. 3545–3553.
- [24] J. T. Springenberg, A. Dosovitskiy, T. Brox, and M. Riedmiller, "Striving for simplicity: The all convolutional net," in *Proceedings of the International Conference on Learning Representations (ICLR)*, San Diego, CA, USA, May 7-9 2015, pp. 1–14. Available: <https://arxiv.org/abs/1412.6806>
- [25] O. Rippel, J. Snoek, and R. P. Adams, "Spectral representations for convolutional neural networks," in *Advances in Neural Information Processing Systems (NIPS)*, C. Cortes, N. D. Lawrence, D. D. Lee, M. Sugiyama, and R. Garnett, Eds. Red Hook, NY, USA: Curran Associates, 2015, pp. 2449–2457.
- [26] R. K. Srivastava, K. Greff, and J. Schmidhuber, "Training very deep networks," in *Advances in Neural Information Processing Systems (NIPS)*, C. Cortes, N. D. Lawrence, D. D. Lee, M. Sugiyama, and R. Garnett, Eds. Cambridge, MA, USA: MIT Press, 2015, pp. 2377–2385.
- [27] F. Agostinelli, M. Hoffman, P. Sadowski, and P. Baldi, "Learning activation functions to improve deep neural networks," in *Proceedings of the International Conference on Learning Representations (ICLR)*, San Diego, CA, USA, May 7-9 2015, pp. 1–9. Available: <https://arxiv.org/abs/1412.6830>
- [28] D. P. Kingma and M. Welling, "Auto-encoding variational Bayes," in *Proceedings of the International Conference on Learning Representations (ICLR)*, Scottsdale, AZ, USA, May 2-4 2013, pp. 1–14. Available: <https://arxiv.org/abs/1312.6114>
- [29] J. Xie, R. Girshick, and A. Farhadi, "Unsupervised deep embedding for clustering analysis," in *Proceedings of the International Conference on Machine Learning (ICML)*, New York, NY, USA, June 20-22 2016, pp. 478–487.
- [30] J. Chang, L. Wang, G. Meng, S. Xiang, and C. Pan, "Deep adaptive image clustering," in *Proceedings of the IEEE International Conference on Computer Vision (ICCV)*, Venice, Italy, October 22-29 2017, pp. 5880–5888. Available: <http://dx.doi.org/10.1109/ICCV.2017.626>

- [31] J. Wu, K. Long, F. Wang, C. Qian, C. Li, Z. Lin, and H. Zha, "Deep comprehensive correlation mining for image clustering," in *Proceedings of the IEEE International Conference on Computer Vision (ICCV)*, Seoul, South Korea, October 27–November 2 2019, pp. 8149–8158. Available: <http://dx.doi.org/10.1109/ICCV.2019.00824>
- [32] J. T. Springenberg and M. Riedmiller, "Improving deep neural networks with probabilistic maxout units," in *Proceedings of the International Conference on Learning Representations (ICLR)*, Banff, Canada, April 14–16 2014, pp. 1–10. Available: <https://arxiv.org/abs/1312.6116>
- [33] N. Srivastava and R. R. Salakhutdinov, "Discriminative transfer learning with tree-based priors," in *Advances in Neural Information Processing Systems (NIPS)*, C. J. C. Burges, L. Bottou, M. Welling, Z. Ghahramani, and K. Q. Weinberger, Eds. Red Hook, NY, USA: Curran Associates, 2013, pp. 2094–2102.
- [34] J. Snoek, O. Rippel, K. Swersky, R. Kiros, N. Satish, N. Sundaram, M. Patwary, M. Prabhat, and R. P. Adams, "Scalable Bayesian optimization using deep neural networks," in *Proceedings of the International Conference on Machine Learning (ICML)*, Lille, France, July 6–11 2015, pp. 2171–2180. Available: <https://arxiv.org/abs/1502.05700>
- [35] D. Mishkin and J. Matas, "All you need is a good init," in *Proceedings of the International Conference on Learning Representations (ICLR)*, San Juan, Puerto Rico, May 2–4 2016, pp. 1–14. Available: <https://arxiv.org/abs/1511.06422>
- [36] J. Zhao, M. Mathieu, R. Goroshin, and Y. LeCun, "Stacked what-where auto-encoders," in *Proceedings of the International Conference on Learning Representations (ICLR)*, San Juan, Puerto Rico, May 2–4 2016, pp. 1–12. Available: <https://arxiv.org/abs/1506.02351>
- [37] J. Yang, D. Parikh, and D. Batra, "Joint unsupervised learning of deep representations and image clusters," in *Proceedings of the IEEE International Conference on Computer Vision and Pattern Recognition (CVPR)*, Las Vegas, NV, USA, June 27–30 2016, pp. 5147–5156. Available: <http://dx.doi.org/10.1109/CVPR.2016.556>
- [38] M. D. Zeiler, D. Krishnan, G. W. Taylor, and R. Fergus, "Deconvolutional networks," in *Proceedings of the IEEE International Conference on Computer Vision and Pattern Recognition (CVPR)*, San Francisco, CA, USA, June 13–18 2010, pp. 2528–2535. Available: <http://dx.doi.org/10.1109/CVPR.2010.5539957>
- [39] A. Coates and A. Y. Ng, "Selecting receptive fields in deep networks," in *Advances in Neural Information Processing Systems (NIPS)*, J. Shawe-Taylor, R. S. Zemel, P. L. Bartlett, F. Pereira, and K. Q. Weinberger, Eds. Red Hook, NY, USA: Curran Associates, 2011, pp. 2528–2536.
- [40] J. Mairal, P. Koniusz, Z. Harchaoui, and C. Schmid, "Convolutional kernel networks," in *Advances in Neural Information Processing Systems (NIPS)*, Z. Ghahramani, M. Welling, C. Cortes, N. D. Lawrence, and K. Q. Weinberger, Eds. Red Hook, NY, USA: Curran Associates, 2014, pp. 2627–2635.
- [41] K. Swersky, J. Snoek, and R. P. Adams, "Multi-task Bayesian optimization," in *Advances in Neural Information Processing Systems (NIPS)*, C. J. C. Burges, L. Bottou, M. Welling, Z. Ghahramani, and K. Q. Weinberger, Eds. Red Hook, NY, USA: Curran Associates, 2013, pp. 2004–2012.
- [42] E. Oyallon, E. Belilovsky, and S. Zagoruko, "Scaling the scattering transform: Deep hybrid networks," in *Proceedings of the IEEE International Conference on Computer Vision (ICCV)*, Venice, Italy, December 7–13 2017, pp. 5619–5628. Available: <http://dx.doi.org/10.1109/ICCV.2017.599>
- [43] K. He, X. Zhang, S. Ren, and J. Sun, "Deep residual learning for image recognition," in *Proceedings of the IEEE International Conference on Computer Vision and Pattern Recognition (CVPR)*, Las Vegas, NV, USA, June 27–30 2016, pp. 770–778. Available: <http://dx.doi.org/10.1109/CVPR.2016.90>